Journal of Geophysical Research: Oceans

RESEARCH ARTICLE
10.1029/2018JC013945

Interannual to Multidecadal Forcing of Mesoscale Eddy Kinetic Energy in the Subtropical Southern Indian Ocean

Andrew S. Delman[1], **Tong Lee**[1], **and Bo Qiu**[2]

[1]Jet Propulsion Laboratory, California Institute of Technology, Pasadena, CA, USA, [2]Department of Oceanography, University of Hawai'i at Mānoa, Honolulu, HI, USA

Key Points:
- Mesoscale eddy activity and sea level in the subtropical southeast Indian Ocean covary on interannual to multidecadal time scales
- The covariability of sea level and mesoscale eddy activity is caused by common remote forcing from the tropical Pacific
- In the subtropical south central Indian Ocean, local wind stress and remotely generated subsurface variability force eddy activity

Correspondence to:
A. S. Delman,
adelman@jpl.caltech.edu

Citation:
Delman, A. S., Lee, T., & Qiu, B. (2018). Interannual to multidecadal forcing of mesoscale eddy kinetic energy in the subtropical southern Indian Ocean. *Journal of Geophysical Research: Oceans*, *123*. https://doi.org/10.1029/2018JC013945

Received 26 FEB 2018
Accepted 23 OCT 2018
Accepted article online 1 NOV 2018

Abstract A region of elevated mesoscale eddy activity spans the subtropical southern Indian Ocean (SSIO) between Madagascar and Australia. The interannual and decadal changes in eddy activity in the SSIO eddy band, as represented by the variability of eddy kinetic energy (EKE), have implications for the large-scale circulation, mixed-layer budgets, and biological activity. An analysis of nearly two and a half decades of sea level anomaly (SLA) data from merged satellite altimetry shows that, in the southeast Indian Ocean east of 90°E, the variations of EKE and SLA are positively correlated on interannual and decadal time scales. Moreover, EKE exhibits a multidecadal increasing linear trend that corresponds to an increasing trend of SLA in the region. The EKE-SLA covariability in the southeast Indian Ocean does not appear to be associated with a preference for anticyclonic over cyclonic eddy activity; rather, it can be attributed to the common remote forcing from the tropical Pacific associated with the El Niño–Southern Oscillation and the Pacific Decadal Oscillation. In the west central SSIO, wind stress curl just south of the eddy band forces potential vorticity anomalies that affect conditions for instability in the west central SSIO; potential density and potential vorticity gradient anomalies also suggest a remote forcing mechanism originating in the region southwest of Australia. The interannual to multidecadal variability of EKE in the SSIO and its relationship with large-scale SLA has implications for mixed-layer dynamics and biogeochemistry and provides a basis for assessment of model simulations of eddy activity in the region.

Plain Language Summary Eddies—rotating *storm systems* in the ocean—that are formed in the parts of the ocean between the tropics and poleward regions are very important for moving heat, salt, and other substances dissolved in the ocean between the tropics and the poles. An area in the southern Indian Ocean between Madagascar and Australia has particularly high levels of eddy activity, and the energy of the eddies changes substantially over the course of years and decades. To understand why these changes occur, satellite data were used that measure the height of the ocean surface and therefore tell us about the ocean circulation and its variability. This study found that levels of eddy activity near Australia are largely determined by the climate phenomena of La Niña and El Niño. In the central part of the southern Indian Ocean, closer to Madagascar, eddy energy levels are influenced by wind variations locally and ocean conditions in the eastern Indian Ocean. These factors that influence eddy activity in the southern Indian Ocean can help us make better predictions of eddy energy in the region; this will tell us more about how heat, salt, and nutrients are transported between the tropics and the waters near Antarctica.

1. Introduction

The 30–20°S latitude range in the Indian Ocean (henceforth referred to as the subtropical southern Indian Ocean or SSIO) is home to a band of elevated sea surface height (SSH) variability due to enhanced eddy activities. This band of enhanced eddy activity spans the entire basin, in contrast to similar bands of enhanced eddy activities in the northern and southern subtropical Pacific Ocean that are mostly confined to the western side of the basin (Figure 1a). Moreover, no such enhanced eddy band is found in the Atlantic Ocean. The SSIO eddies are generated along sharp meridional gradients of temperature and salinity (e.g., Melnichenko et al., 2017), and their latitude range coincides with the downwelling branch of the Indian Ocean shallow overturning circulation (e.g., Lee, 2004; Lee & Marotzke, 1998; Schott et al., 2002). Therefore, interannual and decadal variations in SSIO eddy levels have a potential influence on mixed-layer heat and salt budgets and meridional transports, as well as potential impacts on the large-scale and regional circulation through eddy mean flow interaction. Anticyclonic eddies in the SSIO region are also associated with eddy-induced Ekman

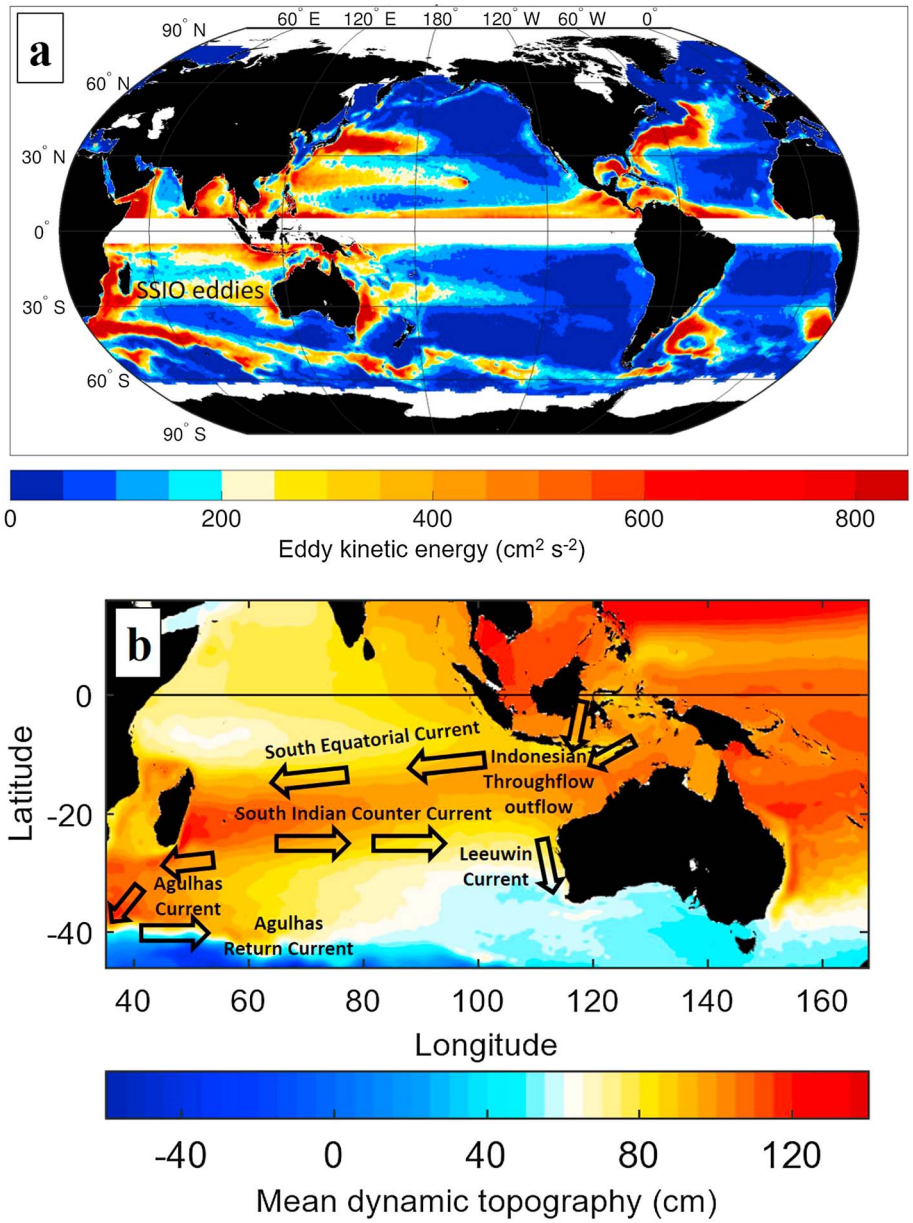

Figure 1. (a) Global time mean eddy kinetic energy computed from CLS SSALTO/DUACS gridded dynamic topography data, 1993–2015; the SSIO eddy band is annotated. (b) Time mean dynamic topography from CLS SSALTO/DUACS data in the southern Indian Ocean region, with major currents in or adjacent to the SSIO region annotated. CLS = Collecte Localisation Satellites; SSIO = subtropical southern Indian Ocean.

upwelling (e.g., Gaube et al., 2013, 2014, 2015), which has a direct impact on biological productivity. Moreover, the changes in mixed-layer vertical and horizontal processes associated with eddy activity (e.g., Chelton & Xie, 2010; Gaube et al., 2013) may be associated with variations of the mixed-layer depth and/or pycnocline depth, for which sea level anomaly (SLA) is a robust indicator in the South Indian Ocean (e.g., Halkides & Lee, 2011; Trenary & Han, 2012, 2013; Xie et al., 2002). Hence, the relationship between SLA and eddy kinetic energy (EKE) has implications for eddy interactions with upper ocean structure and dynamics.

Mesoscale eddy activity in the SSIO extends across the basin (e.g.,Morrow & Birol, 1998; Palastanga et al., 2007), though it is particularly high near the eastern and western boundaries (Figure 1a). Two mechanisms for SSIO eddy generation have been proposed (Table 1). On the eastern side, the eddies are generated by the Leeuwin Current off the west coast of Australia (Figure 1b) through mixed barotropic and baroclinic instability (Batteen & Butler, 1998; Feng et al., 2005) and subsequently radiate offshore toward the west, steered by

Table 1
Some Key References Concerning SLA and Eddy Variability in the SSIO Region

Reference	Time scale(s) analyzed[a]	Key findings relevant to the present study
Batteen and Butler (1998)	IS, A, and M	Mixed barotropic and baroclinic instability in the Leeuwin Current generates mesoscale eddies, which interact to intensify the Leeuwin Current
Morrow and Birol (1998)	SA, A, and IA	Alongshore pressure gradient primarily forces Leeuwin Current and offshore Rossby wave radiation
Potemra (2001)	IS, SA, A, and IA	Equatorial Pacific winds can force coastal Kelvin waves that radiate offshore in the SSIO as Rossby waves
Birol and Morrow (2001)	IS, SA, A, and IA	Baroclinic Rossby waves observed in the SSIO are largely free waves (not locally wind forced), radiating from the eastern boundary
Birol and Morrow (2003)	SA	Quasi-semiannual Rossby waves appear to propagate offshore even south of the turning latitude (27°S), manifesting to some degree as nonlinear eddies
Fang and Morrow (2003)	IS	Mesoscale eddies generated in the Leeuwin Current are steered by topography to follow certain pathways in the SSIO
Morrow et al. (2003)	IS and M	Mesoscale eddies are steered by isopycnal contours and bathymetry, and penetrate to at least 1,500-m depth
Morrow et al. (2004)	IS	Equatorward and poleward deflections of SSIO anticyclonic and cyclonic eddies respectively, especially south of ~25°S
Feng et al. (2005)	IS, A, IA, and M	Anomalous alongshore pressure gradient along eastern boundary of SSIO contributes to instability and eddy generation in the Leeuwin Current
Palastanga et al. (2006)	IA	Interannual variability of mesoscale eddy activity near Madagascar is linked to shifts in the subtropical and tropical gyres, potentially related to the Indian Ocean Dipole
Palastanga et al. (2007)	IS, A, and M	Baroclinic instability from vertical shear between SICC and SEC is responsible for eddy generation in the central SSIO; instabilities generate Rossby waves that become nonlinear eddies
Lee and McPhaden (2008)	IA and D	Interannual and decadal variability of SSH in the northwestern tropical Pacific leads SSH in the eastern SSIO
Jia, Wu, & Qiu (2011)	IA	SSIO EKE (box averaged) is correlated with the Southern Annular Mode; wind stress variations drive geostrophic convergence that changes meridional gradients of temperature and therefore baroclinic instability
Jia, Wu, Lan, and Qiu (2011)	A	EKE in the central SSIO peaks annually during austral summer, driven by meridional Ekman and geostrophic convergences that enhance baroclinic instability
Zheng et al. (2018)	IA	ENSO influences EKE by changing the vertical gradient of meridional velocity near the Leeuwin Current; in the central SSIO, both ENSO and SAM may change the vertical gradient of zonal velocity and affect EKE

Note. SLA = sea level anomaly; SSIO = subtropical southern Indian Ocean; SICC = Subtropical Indian Counter Current; SEC = South Equatorial Current; SSH = sea surface height; EKE = eddy kinetic energy; ENSO = El Niño/Southern Oscillation; SAM = Southern Annular Mode.
[a]Time scales are abbreviated as follows: IS (intraseasonal), SA (semiannual), A (annual), IA (interannual), and D (decadal), M (long-term mean). Manuscripts analyzing the evolution of individual eddies are considered as studying intraseasonal time scales, while manuscripts analyzing eddy energetics are classified according to the time scales of energy/EKE variation considered.

topography and isopycnal contours (Fang & Morrow, 2003; Morrow et al., 2003). Warm core anticyclonic eddies are deflected slightly equatorward, primarily south of 25°S, while cold core cyclonic eddies are deflected poleward (Chelton et al., 2011; Morrow et al., 2004). The second generation mechanism for SSIO eddies predominates in the central and western SSIO, where baroclinic instability is driven by the vertical shear between the eastward Subtropical Indian Counter Current at the surface and the deeper, westward South Equatorial Current (Jia, Wu, & Qiu,2011; Palastanga et al., 2007; Figure 1b). The Subtropical Indian Counter Current is frequently divided into three zonal jets (Menezes et al., 2014), corresponding approximately to preferred

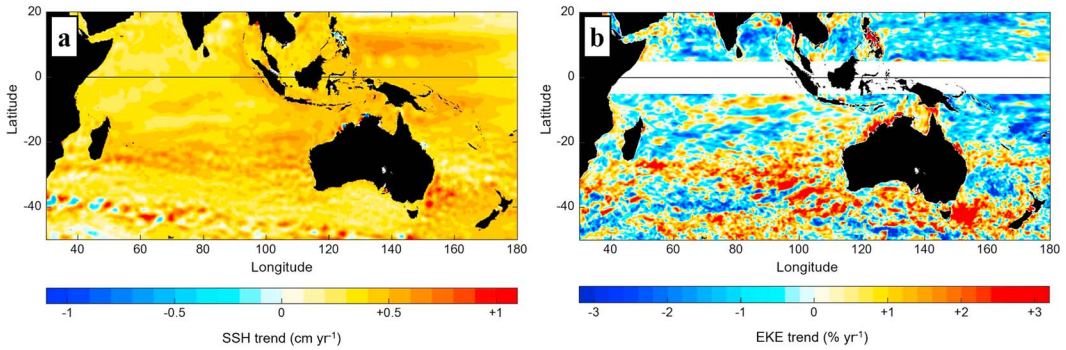

Figure 2. (a) Temporal trend from linear regression of gridded dynamic topography (i.e., sea surface height) data, 1993–2016. (b) Temporal trend of EKE, 1993–2016; the trend is normalized by the time mean EKE at each location (Figure 1a) and expressed as a percentage per year. SSH = sea surface height; EKE = eddy kinetic energy.

pathways of eddy propagation (e.g., Fang & Morrow, 2003). Stability analyses explain the substantial annual cycle of eddy activity in the central and western SSIO (Jia, Wu, & Qiu, 2011; Palastanga et al., 2007).

Despite the attention that has been given to the generation and propagation of individual eddies in the Leeuwin Current, relatively few studies have considered the interannual to multidecadal variation in energy present at oceanic mesoscales across the SSIO eddy band. Birol and Morrow (2001) found that the propagation of linear Rossby waves westward across the SSIO is well explained by SLA eastern boundary forcing, while Birol and Morrow (2003) suggested that coastal wave propagation along the eastern boundary may spur westward radiation of SLA signals even south of the turning latitude for quasi-semiannual waves (25–30°S; Potemra, 2001) with the aid of nonlinear processes. In addition, the phase of the El Niño/Southern Oscillation (ENSO) modulates EKE locally in the Leeuwin Current (Feng et al., 2005; Zheng et al., 2018). An analysis by Jia, Wu, Lan, and Qiu (2011) emphasized the effect of the Southern Annular Mode (SAM) on eddy generation in the eastern SSIO; they also found a connection between the ENSO and SSIO eddy activity, which Zheng et al. (2018) attributed to the vertical gradient (shear) in meridional velocity between the southward Leeuwin Current and the Leeuwin Undercurrent. Far from the Leeuwin Current in the central and western SSIO, Zheng et al. (2018) found weak correlations with vertical shear of horizontal velocity and ENSO, but otherwise, there has not been an explanation of the substantial interannual and decadal variability of EKE in the SSIO interior. The Indian Ocean Dipole (Saji et al., 1999) climate mode influences levels of EKE near Madagascar (Palastanga et al., 2006) but does not significantly correlate with EKE levels in the interior SSIO (Jia, Wu, Lan, & Qiu, 2011; Zheng et al., 2018).

Tropical Pacific forcing is also known to affect large-scale sea level and thermocline depth variability in the southeast Indian Ocean (e.g., Lee & McPhaden, 2008; Trenary & Han, 2013). However, the relationship of eddy variability and large-scale sea level variation in the SSIO, which has implications for mixed-layer dynamics and biogeochemistry, has not yet been investigated. The linear trend of sea level estimated from 24 years of altimeter data (1993–2015; Figure 2a) shows enhanced sea level rise in the SSIO eddy band; moreover, banded structure in the meridional direction and mesoscale structure in the zonal direction are evident in the sea level trends. The 24-year linear trend of EKE (Figure 2b) is positive over most of the SSIO, increasing at the rate of approximately 1–3% per year; the SSIO eddy band also has positive skewness, which can indicate a preference for the generation of anticyclonic over cyclonic eddies (Thompson & Demirov, 2006). The region with positive EKE trend in the SSIO roughly coincides with elevated sea level trends >0.4 cm/year (Figure 2a). This motivated us to investigate the relationship between eddy variability and large-scale sea level change from interannual to multidecadal time scales in the SSIO; specifically, we consider this relationship in the context of interannual and decadal variability and examine the spatial distribution of multidecadal trends in sea level and EKE.

To improve an understanding of the underlying physical processes that cause interannual to multidecadal variations of eddy activities in the SSIO and their relationship to sea level variability, this study assesses several forcing mechanisms of EKE and sea level. These include (1) possible preferential generation of anticyclones versus cyclones and resulting sea level impacts, (2) remote forcing by large-scale climate variability, and (3) locally and remotely generated potential vorticity (PV) and potential density anomalies that affect how favorable conditions are for instability. To achieve this, we first extract the specific component of EKE that

can be attributed to mesoscale motions and verify that these motions account for most EKE in the SSIO eddy band. By considering spatial variations in eddy activity levels within the SSIO eddy band, we confirm that there are at least two largely independent regions of eddy variability in the SSIO eddy band, with distinct forcing mechanisms.

The manuscript is organized as follows: Section 2 discusses the data sets used and the method for separating the SLA fields associated with mesoscale and larger-scale motions. Section 3.1 discusses the relationship between SLA and EKE in the eastern SSIO and assesses the possible contribution of mesoscale EKE to sea level variability. Section 3.2 investigates the influences of large-scale climate modes on SSIO eddy activity, and section 3.3 discusses the propagation of eddy energy and PV/potential density anomalies in the SSIO interior. Section 4 summarizes the main findings and discusses areas for future work motivated by the results of this study.

2. Data and Method

The primary data set analyzed in this study consists of maps of absolute dynamic topography (ADT) produced by Collecte Localisation Satellites (CLS; Ducet et al., 2000). The CLS Segment Sol multimissions of ALTimetry and Orbitography Data Unification and Altimeter Combination System (SSALTO/DUACS) data have a spatial resolution of 0.25° × 0.25° and daily temporal resolution, spanning the years 1993–2015. A low-pass filter is applied to the along-track data prior to the objective mapping procedure that produces the gridded product, attenuating wavelengths shorter than 200 km in the subtropics. The spatial and temporal correlation scales used in the objective mapping procedure also attenuate spatial scales shorter than 200 km and time scales shorter than 10–15 days, and additional accounting for along-track correlated errors may remove some longer-wavelength variability in the real ocean (Ducet et al., 2000). Therefore, we may expect that the substantial number of small eddies in this region with radii smaller than 100 km (Zheng et al., 2015) is not well represented in the gridded CLS data, and other variability not well resolved by multiple satellite tracks may also be inaccurate. Nonetheless, the gridded dynamic topography data from CLS represent the most extensive and spatiotemporally continuous record we have of the near-surface circulation, and its use in this study is consistent with the majority of prior studies of SSIO eddies that have used the same gridded product. The ADT from the CLS data was spatially filtered to compute a low-passed dynamic topography field (ADT_{lp}), using a error function-based spatial low-pass filter applied in the wavenumber domain with a transfer function:

$$E_c(k) = 0.5 - 0.5\,\mathrm{erf}\left(5 \ln \frac{|k|}{k_c}\right) \tag{1}$$

with cutoff wavenumber k_c corresponding to a 6° wavelength in longitude and latitude. This filter is applied in both the zonal and meridional directions to generate ADT_{lp}; the residual ADT_{meso} represents mesoscale motions.

$$ADT_{meso} = ADT - ADT_{lp}. \tag{2}$$

The 6° threshold was chosen based on typical eddy radii of 60–130 km at the latitudes of the SSIO eddy band (e.g., Chelton et al., 2011), corresponding approximately to spatial wavelengths of 2–5°. At this stage the long-term mean of ADT_{lp} and ADT_{meso} is removed to yield the sea level anomaly fields SLA_{lp} and SLA_{meso}. EKE_{lp} is computed from SLA_{lp} as follows:

$$EKE_{lp} = \frac{1}{2}\left|\hat{\mathbf{k}} \times \frac{g}{f}\nabla\left(SLA_{lp}\right),\right|^2 \tag{3}$$

with g being the acceleration of gravity and f the Coriolis parameter.

The EKE_{meso} is computed from SLA_{meso} analogously to (3). For the correlation analyses in this study, the mean, trend, seasonal cycle, and its first harmonic were removed from EKE and its components (as well as SLA), and the filter (1) was applied in frequency space with a cutoff time scale of 14 months. The potential role of ENSO, SAM (also known as the Antarctic Oscillation), and Pacific Decadal Oscillation (PDO) in forcing mesoscale EKE variability was examined using index time series obtained from the website of the National Weather Service's Climate Prediction Center (http://www.cpc.ncep.noaa.gov).

In addition to the CLS dynamic topography data, two other remote sensing-based products and an ocean state estimate were used to investigate sources of mesoscale EKE variability in the interior SSIO. The Mesoscale

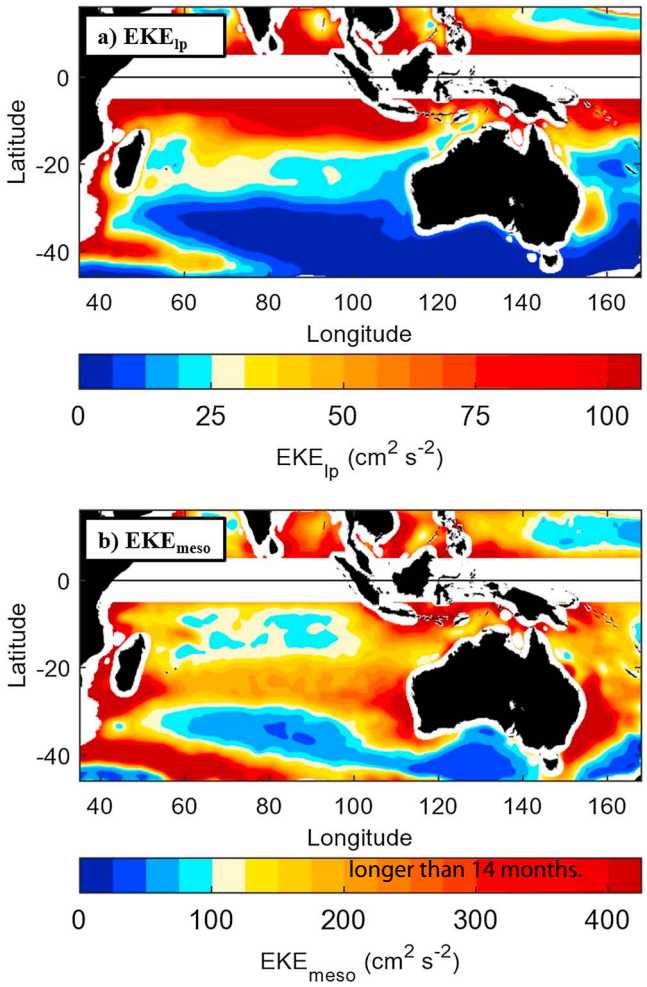

Figure 3. (a) The 1993–2015 time mean values of the surface eddy kinetic energy EKE_{lp} derived from the spatially low passed sea level anomaly SLA_{lp}. (b) The 1993–2015 time mean values of the surface mesoscale eddy kinetic energy EKE_{meso} derived from SLA_{meso}. The contour intervals are 6.25 cm^2/s^2 in (a) and 25 cm^2/s^2 in (b); different contour intervals were chosen for the panels to highlight the spatial distribution of each field in the subtropical southern Indian Ocean. EKE = eddy kinetic energy.

Eddy Trajectory Atlas data set (Chelton et al., 2011) currently produced by CLS and made available through Archiving, Validation, and Interpretation of Satellite Oceanographic Data+ (AVISO+) was used to examine the tracks of individual eddies and the mesoscale EKE associated with them. Remotely sensed wind observations are taken from the Cross-Calibrated Multi-Platform (CCMP) 10-m wind product (Atlas et al., 2011), produced by Remote Sensing Systems with 0.25° × 0.25° spatial resolution and monthly means in the zonal and meridional directions; the data used in the analysis span from January 1993 to December 2014. Lastly, output from the Estimating the Circulation and Climate of the Oceans, Phase II (ECCO2) state estimate is analyzed to examine subsurface density and PV gradients. ECCO2 is produced using a global configuration of the Massachusetts Institute of Technology ocean general circulation model (Marshall et al., 1997) and a least squares fit of the model to satellite and in situ data (Menemenlis et al., 2008; Menemenlis, Fukumori, & Lee, 2005; Menemenlis, Hill, et al., 2005) using the Green's function optimization method (Menemenlis, Fukumori, & Lee, 2005). The mean horizontal spacing is 18 km, with 50 vertical levels and a vertical resolution of 10 m near the surface (Menemenlis et al., 2008) increasing to approximately 60–70 m near 500-m depth; we use ECCO2 output spanning the years 1993–2015 (the same range as the satellite dynamic topography data). The use of ECCO2 in this study is to consider the larger-scale ambient gradients that facilitate eddy generation, so small-scale variability is removed using the density and velocity fields using a Gaussian spatial filter with a 2° *e*-folding radius and 4° cutoff radius. The CCMP wind data and ECCO2 output are temporally filtered in the same way as the gridded dynamic topography data, to focus only on time scales

3. Results

3.1. EKE in the SSIO and Its Relationship to Sea Level Variations

3.1.1. Contributions of Large-Scale and Mesoscale Signals to EKE

The spatially filtered surface EKE fields illustrate the relative contributions of large-scale and mesoscale variability in the tropics and higher latitudes (Figure 3). With the difference between the color scales in Figures 3a and 3b, we note that poleward of 20° latitude, EKE_{lp} is generally an order of magnitude smaller than EKE_{meso}. At middle and high latitudes, the EKE_{lp} is associated with scales that are substantially larger than deformation radii; the generally negligible contribution of linear dynamics to EKE at these latitudes is consistent with a nonlinearity parameter (ratio of the maximum rotational speed around eddies to the eddy translation speed) much greater than 1 at middle and high latitudes (Chelton et al., 2011). In the tropics, EKE_{lp} is nearly comparable to EKE_{meso} in many locations; EKE_{lp} may contain some nonlinear eddy activity in the tropics due to the larger radius of deformation, but the nonlinearity parameters given by Chelton et al. (2011) also suggest that linear dynamics are dominant at these latitudes.

Near the equatorward limit of the SSIO eddy band at 20°S, EKE_{lp} shifts from being a leading-order component of EKE to being an order of magnitude smaller than EKE_{meso}; this is a transition region in which the EKE signature of Rossby waves has a marginal effect. North of 20°S, mesoscale eddy energy is more confined to the eastern part of the basin while the EKE for large scales spans across the basin. South of 20°S, EKE_{meso} is the leading-order component of EKE, though wind- and boundary-forced signals are still evident in the SLA field (Birol & Morrow, 2001). The elevated band of EKE in the 20°–30°S may be attributed mostly to mesoscale EKE, as large-scale EKE tapers off in magnitude south of 20°S (Figure 3a), while mesoscale EKE increases (Figure 3b).

3.1.2. The SLA-EKE Relationship

EKE, determined from the spatial gradient of SLA, accentuates the contribution by mesoscale eddies versus large-scale variations. Mesoscale eddies are usually generated by local instability of the flow field or propagate

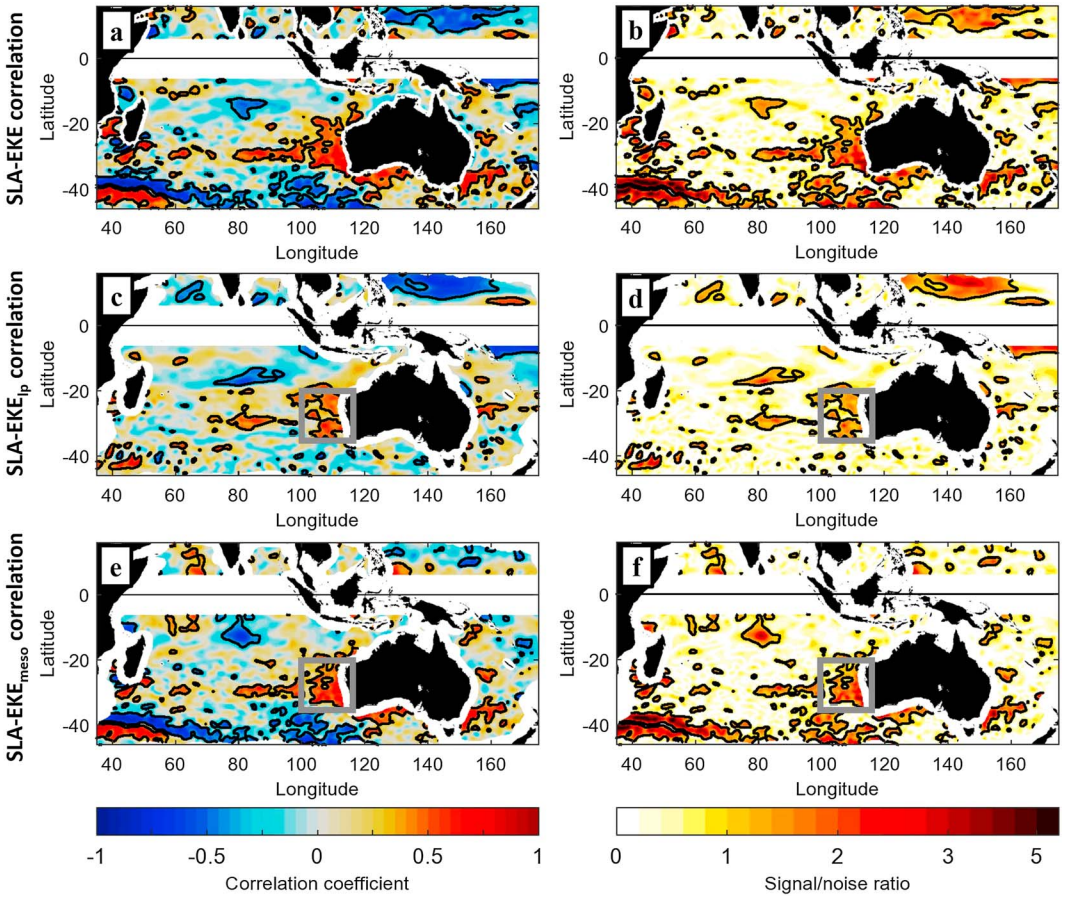

Figure 4. (a) The pointwise temporal correlation coefficient estimate *r* of the total SLA with EKE interpolated to the same grid points, at zero lag. Both fields are spatially smoothed with a Gaussian filter (1° *e*-folding scale, 2° cutoff radius) and temporally low-pass filtered for periods greater than 14 months (interannual/decadal or ID frequencies). The black contour encircles regions in which the signal-to-noise ratio is greater than 1; the signal-to-noise ratio is expressed as the ratio of the magnitude of the correlation coefficient to the magnitude of its (95% confidence) uncertainty. (b) The signal-to-noise ratio for (a). (c–f) Same as (a) and (b) but for the correlations of SLA with EKE_{lp} and EKE_{meso}, respectively. The eastern subtropical southern Indian Ocean box (100°–116°E, 35°–20°S) is indicated in light gray. SLA = sea level anomaly; EKE = eddy kinetic energy.

from another region where they are generated. In some cases mesoscale eddies are modified by or coupled to the wind field. In contrast, SLA itself does not accentuate mesoscale variability over larger-scale variability, and interannual and decadal (ID) SLA variations in the SSIO region typically represent variability in planetary wave pathways (e.g., Lee & McPhaden, 2008).

Hence, from a dynamical standpoint, it is not immediately clear that EKE and SLA would be significantly correlated. However, in the southeast Indian Ocean interannual/decadal (ID) SLA variations are positively and significantly correlated with interannual EKE (Figures 4a and 4b), as well as the spatially filtered EKE_{lp} and EKE_{meso} (Figures 4c–4f). In the northeastern SSIO, the area of robust correlation extends further offshore with EKE_{lp} than with EKE_{meso} (Figures 4c and 4e); however, the correlation with EKE_{meso} is more robust overall throughout the region (Figures 4d and 4f). For the latitude range of 30°–20°S, the positive correlation of EKE-SLA extends 1,000 km or more away from the Leeuwin Current that hugs the west coast of Australia. The time series of EKE and SLA averaged over the eastern tropical Indian Ocean region (35°–20°S, 100°–116°E) further confirms the relationship of EKE and SLA on interannual to decadal time scales (Figures 5a and 5b), and the positive multidecadal trend in both the SLA and mesoscale EKE time series (Figure 5a) echoes the correspondence between the elevated SLA and positive overall EKE trend in the region (Figure 2).

One possible underlying mechanism for the SSH-EKE covariability is the relative dominance of anticyclonic versus cyclonic eddy variability. For example, anticyclonic eddies are associated with positive SLA at oceanic

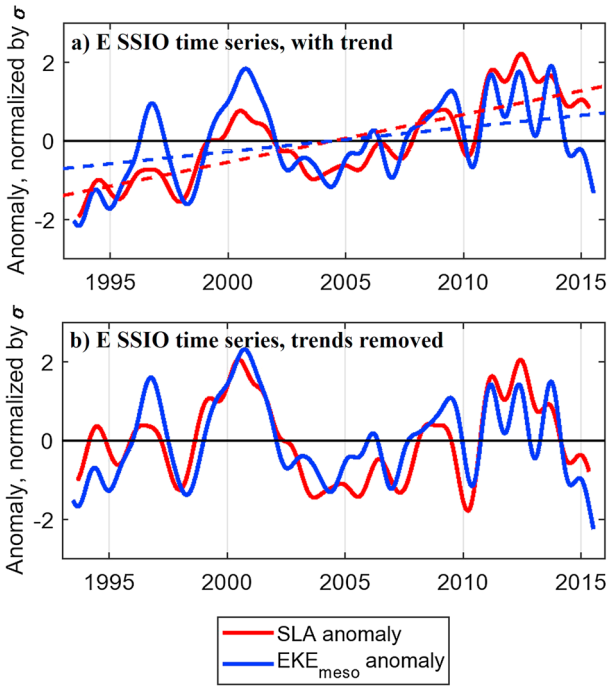

Figure 5. (a) The time series of SLA and EKE_{meso} averaged in the eastern SSIO box with means removed and normalized by their standard deviations. The dashed lines indicate the linear trends regressed to each time series. (b) The time series in (a) with the linear trends removed. The standard deviations are smaller with the trends removed, and therefore, the interannual and decadal variability appears larger in panel (b). SSIO = subtropical southern Indian Ocean; SLA = sea level anomaly; EKE = eddy kinetic energy.

mesoscales. Therefore, if the interannual to multidecadal variaiton of EKE is more dominanted by anticyclonic than cyclonic eddies, then an enhancement of anticyclonic eddy activity would also cause higher SLA, with potential implications for sea level trends (Figure 2). SLA_{meso} represents the sea level variations associated with mesoscale eddies, and therefore, a correlation between SLA_{meso} and EKE_{meso} on ID time scales would indicate that eddy activity may influence ID sea level variability. However, the positive correlation between SLA and EKE_{meso} in the eastern SSIO (Figure 4e) is associated only with the large-scale component of sea level SLA_{lp} (Figures 6a and 6b). There is no substantial contribution from the mesoscale component of sea level in the eastern SSIO, though there is a substantial contribution (negative correlation) from mesoscale sea level south of 35°S (Figures 6c and 6d). Furthermore, we consider whether the time series of mesoscale EKE in the eastern SSIO is driven more by anticyclones or cyclones, by applying a mask to spatially average the mesoscale EKE in positive (anticyclonic) and negative (cyclonic) SLA_{meso} areas separately. This analysis implies that, while cyclonic eddies account for slightly more EKE_{meso} than anticyclones, both types of eddies have comparable contributions to the time variability of EKE_{meso} (Figure 6e). Therefore, the relative contributions of anticyclonic versus cyclonic eddies do not appear to explain the EKE-SLA covariability. One caveat is that mesoscale eddies may nonlinearly interact to impact sea level variations at larger spatial scales, as shown in the North Pacific (Qiu et al., 2015). Therefore, further investigation is necessary to investigate the potential rectification of eddy variability onto background sea level.

The Leeuwin Current generates mesoscale eddies through barotropic and baroclinic instabilities (Batteen & Butler, 1998; Feng et al., 2005; Morrow & Birol, 1998). These eddies radiate westward from the Leeuwin Current region. Therefore, interannual to decadal variability of the Leeuwin Current might also induce variability of eddy activity on the same time scales for some distance away from the eastern boundary. The Leeuwin Current strength is controlled in large part by the pressure gradient along the Australian coast (e.g., Feng et al., 2005; Smith et al., 1991; Thompson, 1987); that is, a higher-pressure difference along the coast between the tropics and midlatitudes would drive a stronger current.

To examine the possible copropagation of nonseasonal anomalies of sea level and EKE, we consider Hovmöller diagrams of SLA and EKE extending across the Indian Ocean in three latitude bands (35°–30°S, 30°–25°S, and 25°–20°S; Figure 7). Pulses of strongly positive and negative EKE_{meso} anomalies originating from the eastern boundary coincide with positive and negative sea level anomalies respectively. Higher SLA at the eastern boundary is associated with a stronger and more unstable Leeuwin Current (Batteen & Butler, 1998; Feng et al., 2005), which supports the generation of mesoscale eddies that propagate westward (Morrow & Birol, 1998). In the eastern SSIO, these pulses of elevated (reduced) eddy activity and higher (lower) EKE propagate in phase with positive (negative) SLA associated with boundary-forced Rossby waves (e.g., Birol & Morrow, 2001). In the interior beyond 100°E, the SLA signals become somewhat decoupled from EKE_{meso} variations. For example, strongly positive SLA (from downwelling Rossby waves) in the middle of the basin during 2001–2003 is coincident with positive EKE_{meso} (higher mesoscale eddy activity) in the same region, but positive SLA during 2009–2010 is coincident with negative or neutral EKE_{meso} (Figures 7b and 7c, and 7e and 7f). This decoupling behavior of interior EKE and SLA indicates that factors other than the radiation of eddies and waves from the Leeuwin Current region contribute to the interior EKE variability.

Since the SLA near the Leeuwin Current region is linked to the SLA in the northwestern tropical Pacific via coastal Kelvin wave propagation through the Indonesian Archipelago (e.g., Cai et al., 2005; Lee & McPhaden, 2008), we examine the relationship of interannual EKE in the eastern SSIO with interannual SLA in the Indo-Pacific region using an optimal correlation method. In this optimal correlation analysis, correlations are computed between a single time series (in this case EKE averaged in the eastern SSIO) and the time series at each point in a spatial domain (in this case, SLA in the Indo-Pacific region). The correlations are computed with

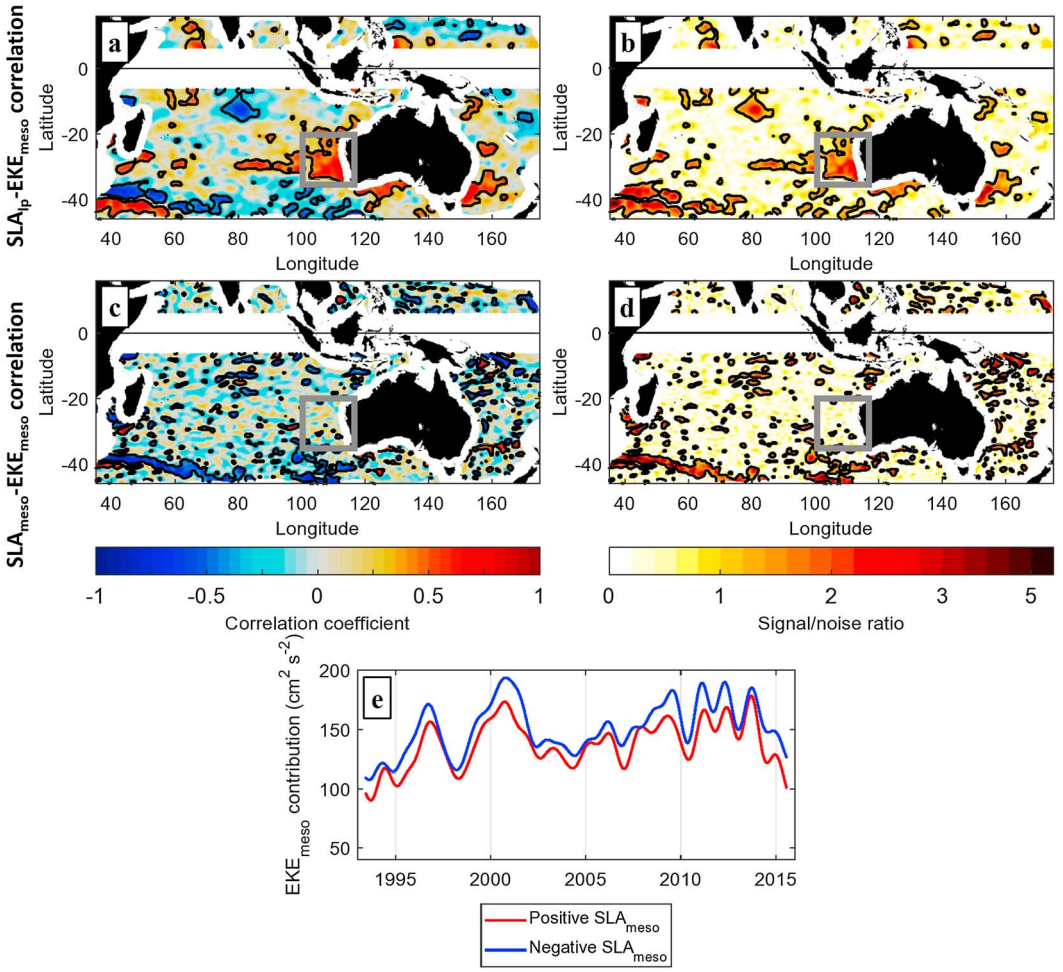

Figure 6. (a, b) Same as Figures 4e and 4f but for the zero-lag correlation of SLA_{lp} with EKE_{meso}. (c, d) Same as (a) and (b) but for the zero-lag correlation of SLA_{meso} with EKE_{meso}. (e) Time series of contributions to EKE_{meso} in the eastern SSIO (gray box in a–d) from areas with positive (negative) SLA_{meso}, computed by setting to zero the EKE_{meso} in areas with negative (positive) SLA_{meso} and spatially averaging in the eastern SSIO box. SSIO = subtropical southern Indian Ocean; SLA = sea level anomaly; EKE = eddy kinetic energy.

SLA at each point leading the time series of eastern SSIO EKE by time intervals in the range 0–2 years; the lag (or lead time) at each point associated with the maximum magnitude correlation coefficient is the *optimum* lag (lead) time. This method resembles the partial lag-regression method used by Wijffels and Meyers (2004) in that it produces maps of optimum coefficients and lags (or lead times); it differs in that we consider only one index at a time (in this case eastern SSIO EKE) and compute correlation rather than regression coefficients. The optimum correlation coefficient, lead time, and signal-to-noise ratio for each point SLA are shown in Figure 8.

Results of the optimal correlation analysis show that the mesoscale EKE near the eastern boundary of the SSIO is robustly correlated with SLA over a broad area of the tropical Indo-Pacific warm pool (Figure 8a). The optimal lead times of the correlation of SLA in the western tropical Pacific relative to eastern SSIO EKE_{meso} range from near zero to about a year (Figure 8b). The 6- to 12-month lead times are consistent with the time scales of wave propagation from the northwestern tropical Pacific (Cai et al., 2005) through the Indonesian Seas and radiation westward from the Australian coast. The near-zero lead times in the southwestern tropical Pacific are likely the result of thermocline anomalies in that area lagging the northern tropical Pacific (Cai et al., 2005; Lee & Fukumori, 2003) and do not represent a direct physical forcing of the SSIO EKE by southwest tropical Pacific wind forcing. In the tropical Indian Ocean near 10°–15°S and 100°–120°E, there is a band with a robust correlation (Figure 8a). However, the lead time for SLA correlation in this area is nearly zero (Figure 8b), as opposed to SLA correlation in the northwest Pacific, which is robust at a lead time of 6 months (Figure 8c). SLA in this region is also closely linked to western tropical Pacific SLA and winds (Lee & McPhaden, 2008);

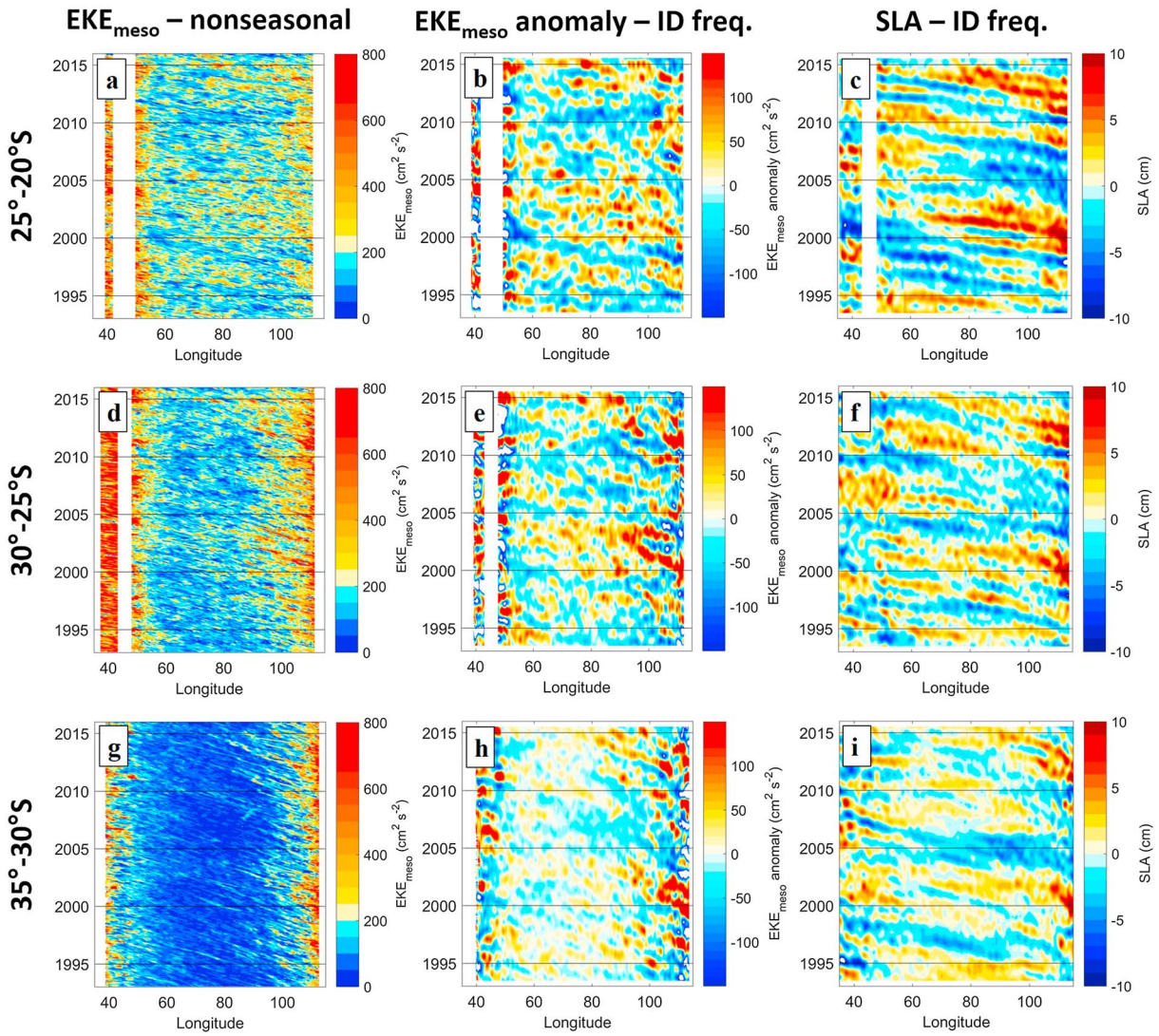

Figure 7. (a) Hovmöller diagrams of EKE_{meso} at nonseasonal frequencies, averaged in the latitude band 25°–20°S; the seasonal cycle is removed but the long-term mean and trend retained, and the data low-pass filtered to capture signals at periods >48 days associated with mesoscale eddies. (b) The EKE_{meso} anomaly in the 25°–20°S band, with the long-term mean, trend, and seasonal cycle removed and low-pass filtered for ID frequencies (periods >14 months). (c) SLA in the 25°–20°S band, filtered for ID frequencies with the mean, trend, and seasonal cycle removed. (d–i) Same as (a)–(c) but averaged in the latitude bands (d)–(f) 30°S–25°S and (g)–(i) 35°–30°S. EKE = eddy kinetic energy; SLA = sea level anomaly; ID = interannual and decadal.

hence, the robust correlation with SLA in the tropical Indian Ocean does not represent a direct causal link with SSIO EKE_{meso} but rather a remote forcing from the western tropical Pacific that influences variability in both regions. The lagged correlation of eastern SSIO EKE_{meso} with scatterometer observations of wind stress curl in the Pacific (not shown) is qualitatively similar, emphasizing that mesoscale eddy activity east of 100°E is strongly influenced by wind forcing of the Rossby waveguide in the Pacific just north of the equator.

The coastal propagation and offshore extent of the signal originating in the northwestern tropical Pacific are all the more apparent when considering the interannual and decadal response of EKE_{meso} regressed onto SLA averaged in the northwestern tropical Pacific (5°–10°N, 140°–160°E; Figure 9). Mesoscale EKE exhibits a weakly positive, coastally trapped response along the edge of the northwestern Australian shelf to tropical Pacific SLA values that are 1 standard deviation above the mean (Figure 9a). However, when the effect of the Pacific forcing reaches the EKE_{meso} maximum south of 25°S (Figure 3b), the EKE_{meso} response to Pacific SLA contribution also reaches a maximum. The ratio of the regressed EKE_{meso} to its uncertainty is greater than 2 near the coast (Figure 9b), indicating a robust contribution in the Leeuwin Current region that lags the Pacific SLA by 3–6 months (Figure 9c). Due west of the maximum in the EKE_{meso} response along the southwestern

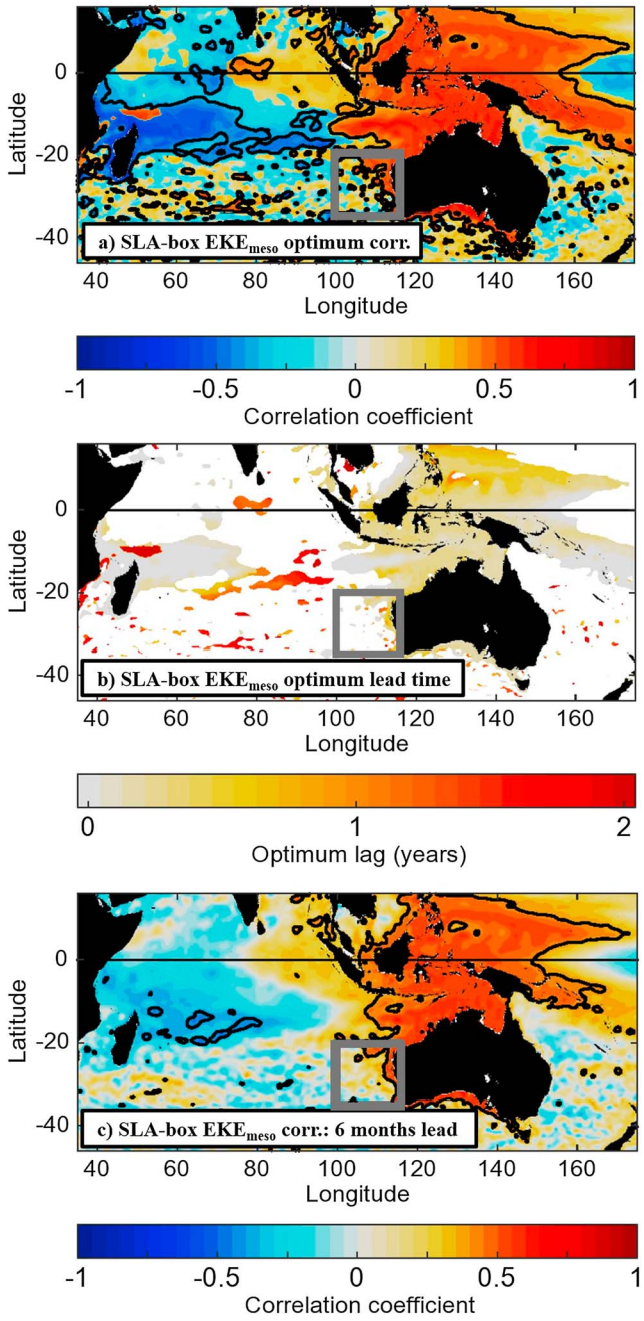

Figure 8. (a) The optimum (maximum magnitude) correlation coefficient of SLA in the Indian Ocean and southwestern Pacific with EKE_{meso} averaged in the eastern SSIO region (gray box), with SLA leading eastern SSIO EKE_{meso} by 0–2 years. Both fields have been temporally low passed for interannual and decadal frequencies; the black contour encircles regions with a signal-to-noise ratio greater than 1 as in Figures 4 and 6. (b) The optimum lead time of SLA relative to eastern SSIO EKE_{meso}. (c) The correlation coefficient of SLA, leading EKE_{meso} in the eastern SSIO region by a fixed 6-month lead time. SLA = sea level anomaly; EKE = eddy kinetic energy; SSIO = subtropical southern Indian Ocean.

Australian coast, the signal also contributes to EKE_{meso} propagating offshore to about 100°E (Figure 9a) with robust signal-to-noise ratios of 1.5–2 (Figure 9b). The lags of 18 months to 2 years for this offshore region of EKE_{meso} (Figures 9c and 9d) are consistent with the ~3–5 cm/s westward eddy propagation from the coast (Chelton et al., 2011; Fu, 2009). However, to the north in the equatorward portion of the SSIO eddy band, the Pacific SLA contribution dissipates quickly offshore (Figure 9a).

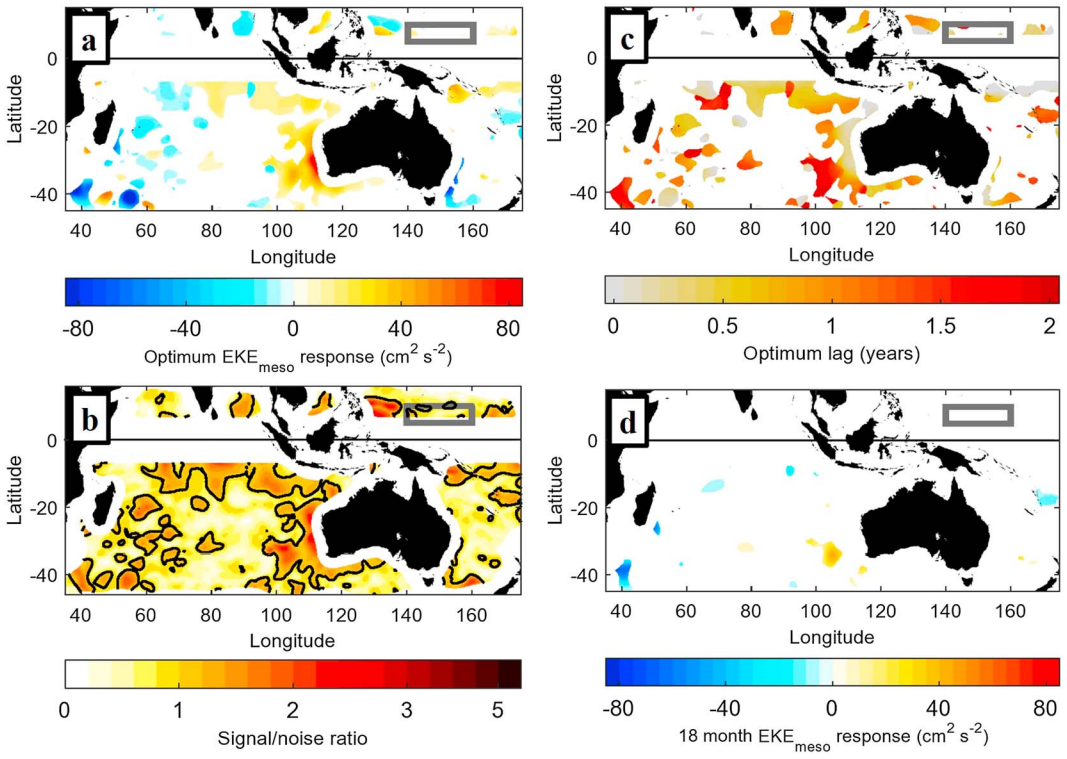

Figure 9. (a) The interannual and decadal-time scale EKE_{meso} response ($R\sigma_{SLA}$, with R the linear regression coefficient of box-averaged temporally detrended SLA onto detrended EKE_{meso}) to SLA values 1 standard deviation above the mean, averaged in the northwestern tropical Pacific (gray box). The response is plotted at optimum lag with NW tropical Pacific SLA leading EKE_{meso} by 0–2 years. The EKE_{meso} field was smoothed with a Gaussian spatial filter (2° *e*-folding radius, 4° cutoff radius) prior to computing the regression; only areas where the signal-to-noise ratio of the regression coefficient is greater than 1 are shaded. (b) The signal-to-noise ratio associated with the optimum EKE_{meso} response in (a). (c) Optimum lag associated with the EKE_{meso} response in (a). (d) The EKE_{meso} response at 18-month lag relative to NW tropical Pacific SLA. EKE = eddy kinetic energy; SLA = sea level anomaly.

3.2. Forcing Associated With Climate Modes

The relationship of the northwestern tropical Pacific SLA and mesoscale EKE in the eastern SSIO region suggests that ENSO or decadal variability in the tropical Pacific can induce variations of eddy activity in the SSIO, a hypothesis supported by the influence of ENSO on the strength of the Leeuwin Current (Feng et al., 2003) where much of the eddy generation occurs. Jia, Wu, Lan, and Qiu (2011) discussed a significant negative correlation between spatially averaged EKE_{meso} in the southeast Indian Ocean and the SAM, while Zheng et al. (2018) explored the influence of ENSO on eddy activity in the SSIO. However, the westward extent of the influence of climate modes on EKE_{meso} has not been clearly mapped, and the climate influence on SSIO mesoscale eddy activity has not been assessed on decadal to multidecadal time scales. Here we consider the relationship of ENSO, SAM, and the PDO to mesoscale EKE across the SSIO eddy band, on interannual to multidecadal time scales.

The Niño3.4 index is negatively correlated with EKE_{meso} in much of the tropical southern Indian Ocean and along the Australian coast (Figure 10a), with signal/noise ratios in many of these regions greater than 2 (Figure 10b). However, in the latitude range of the SSIO eddy band the robust correlations are mostly found east of 100°E. Optimum lags indicate that EKE_{meso} near the Australian coast lags ENSO by only 3–6 months; these lags quickly increase to ~1 year in the NW corner of the eastern SSIO (E SSIO) box and ~1.5 years in the SW corner (Figure 10b), consistent with the range of 3.5- to 10-cm/s westward Rossby wave propagation speeds expected at the latitudes of the NW and SW corners of the box (Chelton et al., 2011).

SAM is generally negatively correlated with mesoscale EKE in the SSIO, though in much of the central and western SSIO the correlation is not particularly robust (Figure 10d); the most robust correlation is limited to a narrow band spanning approximately 30°–25°S and ~95°–105°E (Figure 10e). Optimum lags between SAM and EKE_{meso} are mostly in the 0- to 6-month range, though a couple areas of 12- to 18-month lag are present in

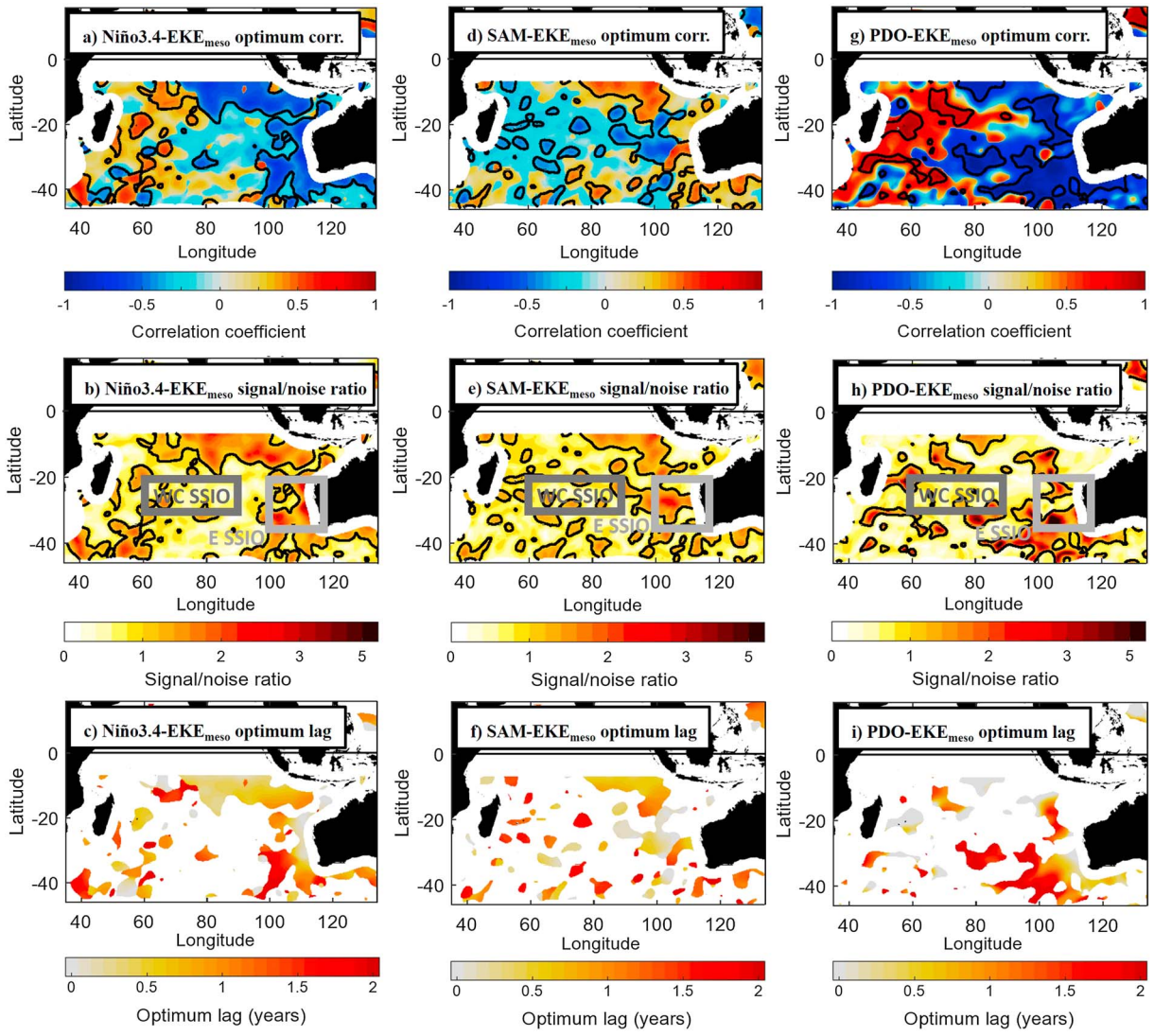

Figure 10. (a) Optimum correlation coefficient of the Niño3.4 index with EKE_{meso} in the Indian Ocean region, at interannual and decadal frequencies, with Niño3.4 leading EKE_{meso} by 0–2 years. The EKE_{meso} field was smoothed with a Gaussian spatial filter as in Figure 9. (b) The signal-to-noise ratio of the optimum correlation coefficient in (a); gray boxes indicate regions that are analyzed in Figure 11. (c) Optimum lag of the EKE_{meso} correlation relative to the Niño3.4 index; regions with a signal-to-noise ratio less than 1 are masked out. (d–f) Same as (a)–(c) but for the correlation of the SAM index with EKE_{meso}. (g–i) Same as (a)–(c) but for the correlation of the PDO index (low-pass filtered for periods longer than 5 years) with EKE_{meso}. EKE = eddy kinetic energy; PDO = Pacific Decadal Oscillation; SAM = Southern Annular Mode.

the western part of the eddy band (Figure 10f). Of note, the region where EKE_{meso} is most robustly correlated with SAM was also the focus of the instability analysis by Jia, Wu, Lan, and Qiu (2011), which suggested that EKE variability in the SSIO is driven by vertical shear of zonal velocity associated with SAM. The localized influence of SAM at 30°–25°S near 100°E may have some importance for mesoscale EKE variability, as this region is in a transition zone between the eastern boundary and interior sections of the SSIO eddy band. However, the direct influence of SAM on EKE_{meso} does not appear to propagate westward beyond ~90°E.

To focus on the decadal influence from the Pacific, the spatial distribution of EKE_{meso} is considered relative to the PDO index (Mantua et al., 1997), which has been low-pass filtered for periods longer than 5 years only, as opposed to the 14-month threshold for other time series. The relationship between the Pacific forcing and EKE_{meso} in the southeastern Indian Ocean is exceedingly robust for these longer time scales, with correlation coefficients less than −0.8 (Figure 10g) and signal-to-noise ratios greater than 5 in some areas (Figure 10h). A similar analysis (not shown) with the Niño3.4 index filtered for longer than 5-year time scales shows a very similar spatial distribution of the correlations, though slightly less robust than the PDO-EKE_{meso} correlations,

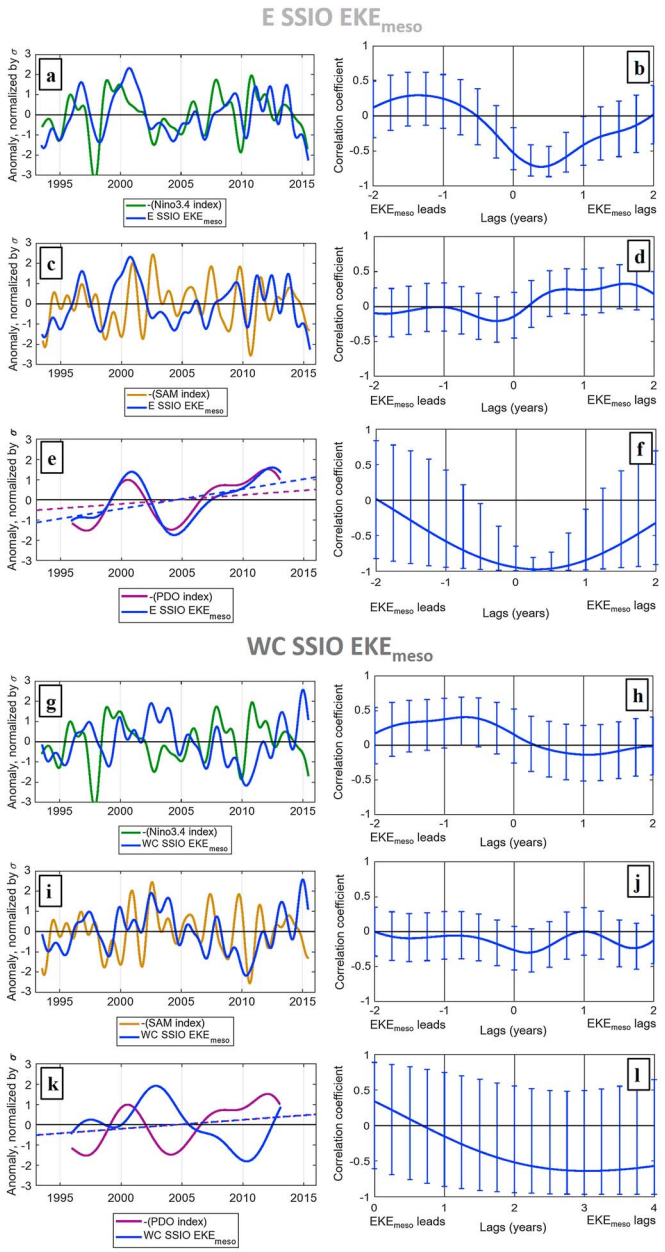

Figure 11. (a) Time series of the Niño3.4 index (with sign reversed) and EKE_{meso} averaged in the eastern SSIO (E SSIO) box as indicated in Figure 10; the time series have had means, trends, and the seasonal cycle removed and have been low-pass filtered for interannual and decadal frequencies. (b) Lagged correlations of Niño3.4 with the EKE_{meso} time series in (a), with 95% uncertainty bounds in the estimate of the correlation coefficient indicated. (c and d) Same as (a) and (b) but for the SAM index with sign reversed. (e and f) Same as (c) and (d) but for the PDO index low-pass filtered for periods longer than 5 years, with sign reversed; in (e) the linear trends are retained in the time series and are also indicated by the dashed lines. (g–l) Same as (a)–(d) but the EKE time series are averaged in the west central SSIO (WC SSIO) region. Panel (l) focuses on EKE_{meso} lagging the PDO index of 0–4 years to show the slightly greater magnitude correlations at longer lags. SSIO = subtropical southern Indian Ocean; EKE = eddy kinetic energy; SAM = Southern Annular Mode; PDO = Pacific Decadal Oscillation.

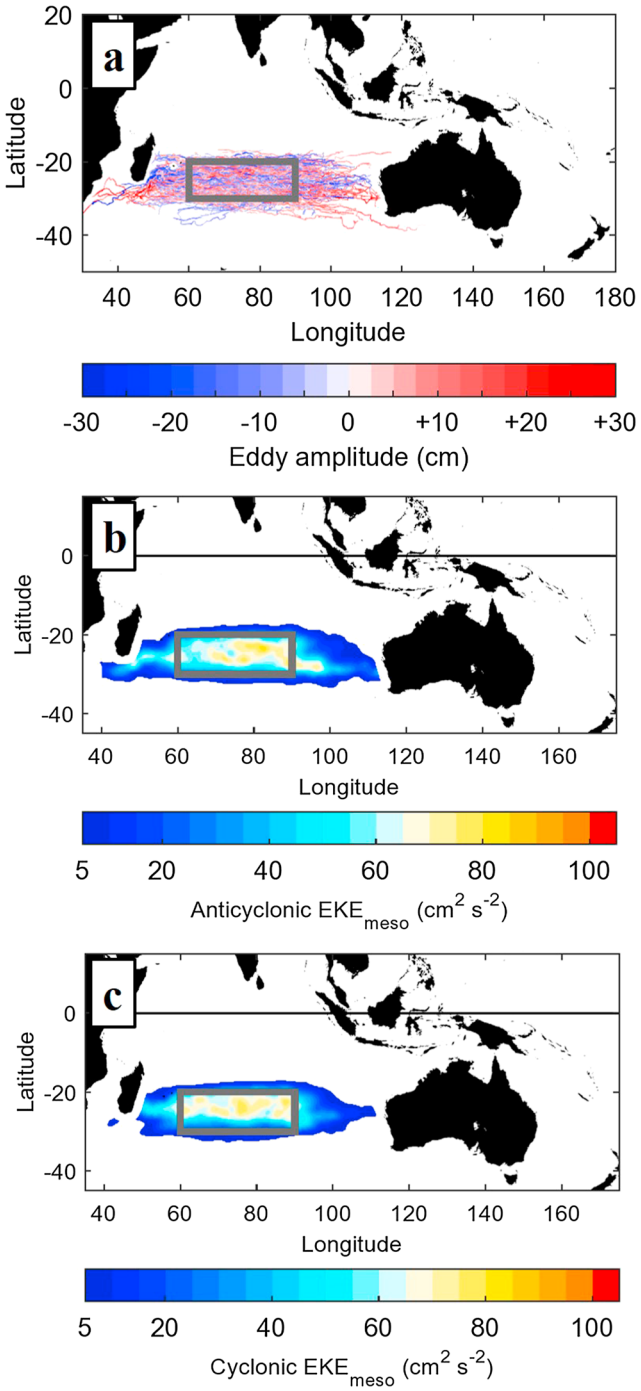

Figure 12. (a) Eddy tracks of time length ≥16 weeks that pass through any part of the WC SSIO region (gray box). Tracks are color coded by sign and amplitude. (b) Time mean EKE_{meso} associated with anticyclone tracks that pass through any part of the WC SSIO region; only regions where the EKE_{meso} is greater than 5 cm^2/s^2 are shaded. (c) Same as (b) but for cyclone tracks. WC = west central; SSIO = subtropical southern Indian Ocean; EKE = eddy kinetic energy.

implying that we can not decisively separate the influence of the PDO from the decadal variability of ENSO. The influence of decadal tropical Pacific forcing can be traced clearly as far west as 80°E and with lags of 2 years or greater, though the dominant influence of the PDO skews southward outside of the SSIO eddy band to the west of 100°E (Figure 10i). This suggests that decadal variability in the SSIO eddy band to the west of 100°E may be forced by other mechanisms.

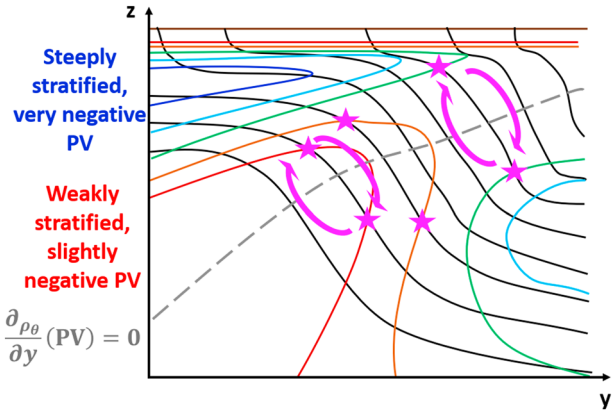

Figure 13. A schematic illustration of an ocean state in the Southern Hemisphere that is susceptible to baroclinic instability. The black contours are potential density surfaces, while (Ertel) PV is indicated by color contours. The gray dashed line indicates the zero crossing in the along-isopycnal meridional gradient of PV that serves as a locus for instability growth, while magenta stars and arrows indicate the exchange of water parcels permitted by this setup. PV = potential vorticity.

We also examined the lagged correlations of the climate mode indices with mesoscale EKE averaged in the eastern SSIO and west central SSIO (Figure 11), in order to consider the aggregate impact of the climate modes in these distinct regions of mesoscale eddy variability. The time series of eastern SSIO EKE_{lp} and EKE_{meso} is closely aligned with the Niño3.4 index (Figure 11a), and the negative Niño3.4-EKE_{meso} correlation is very likelyless than −0.5 at lags of 3–6 months (Figure 11b), indicating a very robust influence from ENSO as Zheng et al. (2018) found. However, despite the localized negative correlation of SAM in part of the E SSIO region, there is no significantly robust correlation between SAM and EKE_{meso} in the E SSIO region overall (Figures 11c and 11d), implying the dominance of the ENSO influence in this region. On decadal time scales, the PDO has a remarkably robust influence on E SSIO EKE_{meso} variability at a 3- to 6-month lead time (Figures 11e and 11f), even considering the influence of Pacific sea level on EKE_{meso} discussed in section 3.1. In the west central SSIO region, the influence of ENSO on EKE_{meso} dissipates (Figures 11g and 11h); the highest-magnitude correlation is with EKE_{meso} leading Niño3.4 by ∼9 months, but there is no known mechanism for such a connection. SAM has a negative correlation leading west central SSIO by 2–3 months (Figure 11j); however, its magnitude is not very impressive, and the time series comparison suggests that SAM is not likely to be a leading-order contributor to mesoscale EKE variability in the region (Figure 11i). The PDO does not appear to contribute robustly to decadal EKE_{meso} variability west of 90°E (Figures 11k and 11l), even though the magnitude of the correlation estimate does increase with increasing lead times for the PDO EKE_{meso}, peaking at 3–4 years (Figure 11l). The very close agreement between the multidecadal linear trends of the PDO and west central SSIO EKE_{meso} (Figure 11k) is likely a coincidence given the lack of any robust connection in the decadal variability (Figure 11l). However, it is very possible that PDO-like variability influences eddy activity across the SSIO eddy band on longer than decadal time scales given the close agreement of the elevated SLA and EKE multidecadal trend maps (Figure 2), and this topic warrants further investigation.

3.3. Forcing of EKE Variability in the West Central SSIO

In contrast to the previous sections 3.1 and 3.2 that focused mostly on EKE in the eastern SSIO region, we now consider mesoscale EKE variations in the interior (west central) SSIO. Like the eastern SSIO, the interior SSIO is influenced by large interannual current variability (Menezes et al., 2016) and unstable dynamics (Palastanga et al., 2007); however, the mesoscale EKE characteristics and variability are distinct from those in the eastern SSIO and do not appear to be influenced substantially by ENSO or SAM. Here we use the trajectories of tracked individual eddies, as well as an analysis of subsurface density and PV gradients, to examine possible sources of mesoscale EKE interannual and decadal variability in the west central SSIO.

3.3.1. Mesoscale EKE Propagation Associated With Individual Eddies

Using the Mesoscale Eddy Trajectory Atlas, the mesoscale EKE contained within individual eddy radii can be quantified; this *tracked eddy* EKE_{meso} is further subdivided into contributions from anticyclonic and cyclonic eddies. EKE_{meso} at a given point (x, y, t_0) is attributed to an individual eddy as follows:

$$\mathrm{EKE}_{\mathrm{eddy}}(x, y, t_0) = \delta(x, y, t_0)\,\mathrm{EKE}_{\mathrm{meso}}(x, y, t_0), \tag{4}$$

where $\delta(x, y, t_0) = 1$ if the point is contained within a radius L of the eddy center (x_0, y_0) at time t_0, and 0 otherwise. L is taken to be equal to 1.4 L_s, the speed-based eddy scale as described in Chelton et al. (2011); 1.4 L_s is also an approximation of the effective radius L_{eff} defined by Chelton et al. (2011). This formulation differs somewhat from the one Chelton et al. (2011) used to quantify the EKE associated with individual eddies, as we assume that the mesoscale EKE contribution eddy can be approximated by considering the eddy as a circle. While eddies themselves do not always have circular shapes, there is no reason to think that the anticyclonic and cyclonic EKE_{meso} calculations here are biased by this approximation, which is considered preferable to implementing the time-intensive contouring approach used by Chelton et al. (2011) to define eddy perimeters. As our eddy approximations do not correspond to closed contours of SSH, it is possible that a point (x, y, t_0) may be located within multiple N eddy radii. In these cases, the EKE_{meso} at that point is divided equally between each eddy; that is, $\delta = 1/N$ for each eddy. Using this methodology, we found 60–80% of the total

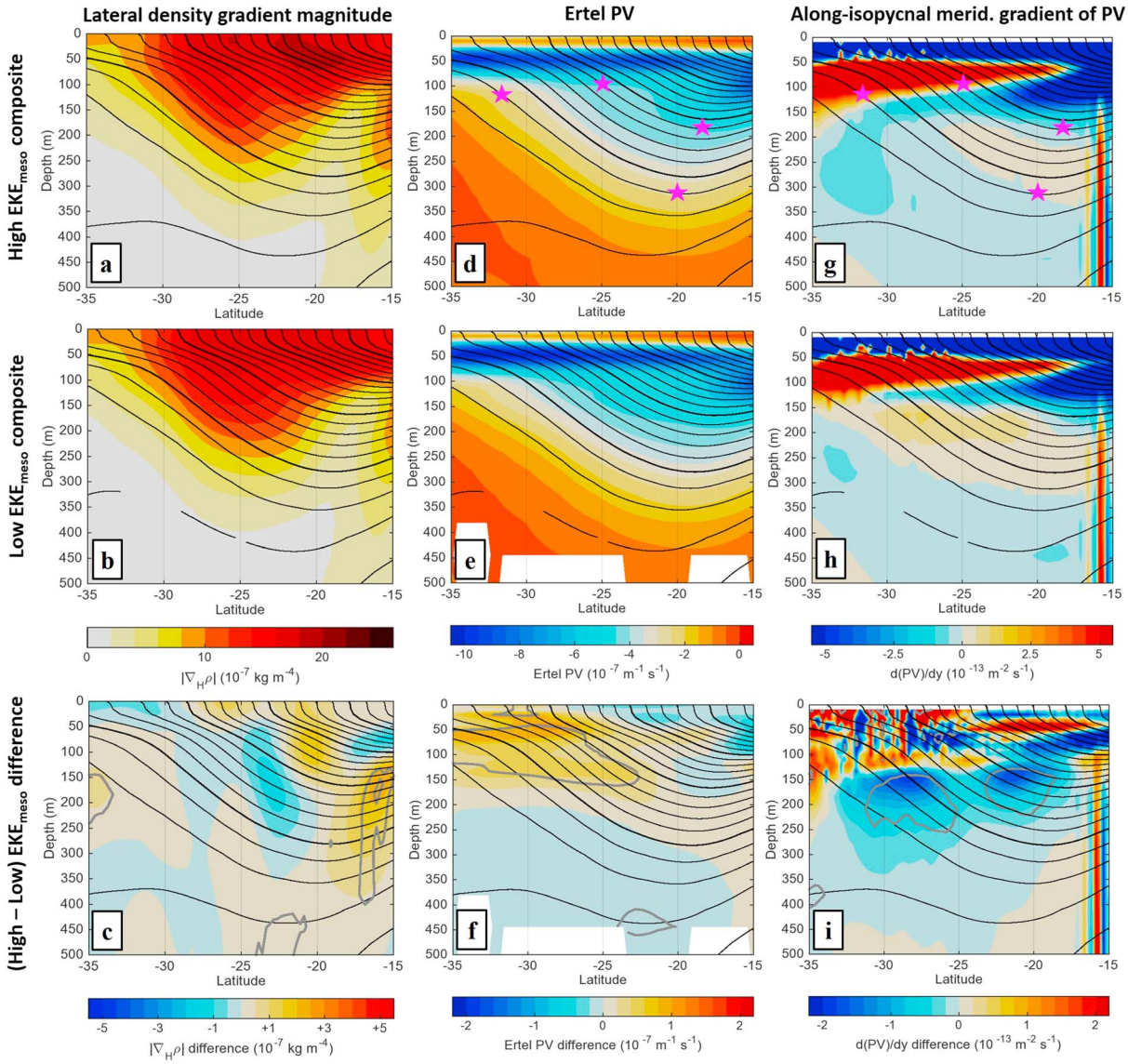

Figure 14. (a) High EKE$_{meso}$ composite meridional transect of the lateral density gradient magnitude $|\nabla_H \rho|$, zonally averaged 60°–90°E, and temporally averaged for periods leading WC SSIO EKE$_{meso}$ anomalies > 0.5σ by 6 months. The black contours indicate composite isopycnals (contour interval of 0.2 kg/m^3), with thicker contours every 1 kg/m^3. (b) Same as (a) but averaged in time periods leading WC SSIO EKE$_{meso}$ anomalies < −0.5σ by 6 months. (c) Difference of high EKE$_{meso}$ composite (a) minus low EKE$_{meso}$ composite (b). The gray contours indicate composite differences with a signal-to-noise ratio greater than 1; the noise is equal to the combined uncertainty of the high and low EKE$_{meso}$ composite averages, determined using bootstrap averaging (n = 1,000) of random composites of similar time lengths. (d–i) Same as (a)–(c) but for composites of (d)–(f) Ertel PV and (g–i) the AIM gradient of Ertel PV. Magenta stars in (d) and (g) indicate the bounds of potential instability development implied by the isopycnal slopes and AIM PV gradients. Areas with missing shading or contours indicate locations with insufficient data to accurately constrain the zonal and temporal averages. AIM = along-isopycnal meridional; PV = potential vorticity; EKE = eddy kinetic energy; SSIO = subtropical southern Indian Ocean; WC = west central.

EKE$_{meso}$ in the SSIO to be contained within eddy contours and therefore attributable to tracked anticyclonic or cyclonic eddies.

Though the EKE$_{meso}$ variability in this region is distinct from that in the eastern SSIO, a number of eddies from the Leeuwin Current region do travel westward and reach the west central SSIO (Figure 12a). Of these Leeuwin Current eddies, two distinct bands can be seen extending westward to at least 100°E: a band dominated by cyclones near 25°S and a band dominated by anticyclones to the south of it. When considering the EKE$_{meso}$ associated with these eddy tracks, however, it is apparent that most of the EKE$_{meso}$ in the west central SSIO is not associated with these Leeuwin Current-sourced eddies (Figures 12b and 12c). Only about 20–25 cm^2/s^2 of time mean EKE$_{meso}$ in the Leeuwin Current is associated with anticyclones that will reach the west central SSIO

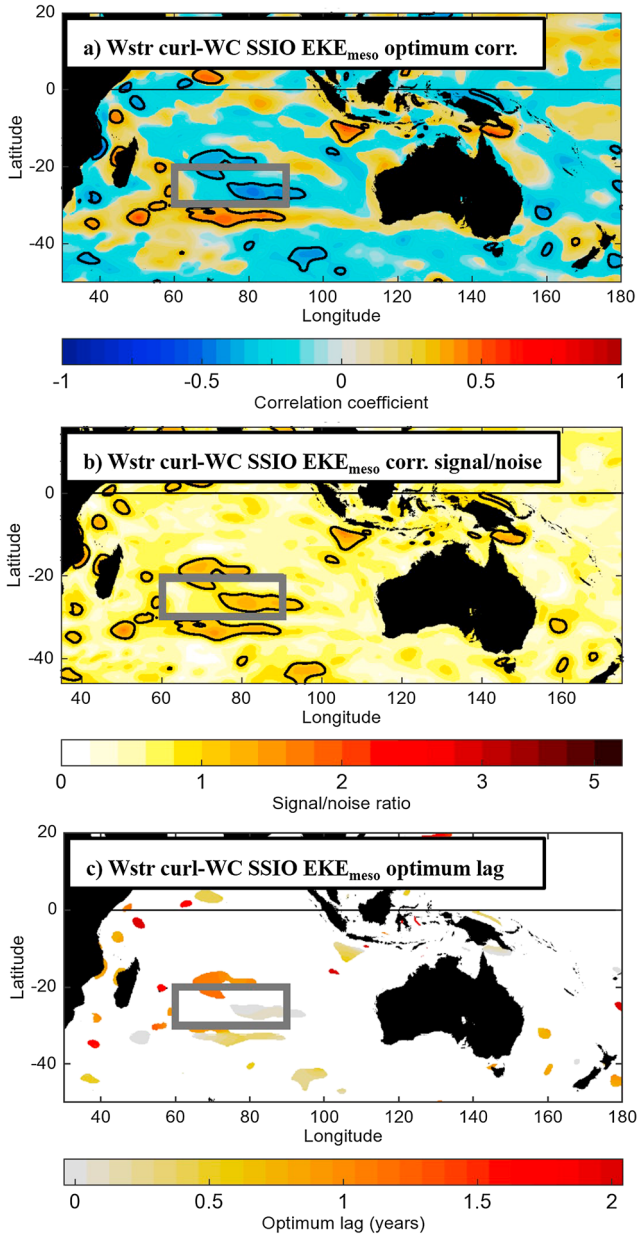

Figure 15. (a) The optimum (maximum magnitude) correlation coefficient of Cross-Calibrated Multi-Platform wind stress curl with EKE_{meso} averaged in the west central SSIO region (gray box), with wind stress curl leading WC SSIO EKE_{meso} by 0–2 years. Both fields have been temporally low passed for interannual and decadal frequencies; the black contour encircles regions with a signal-to-noise ratio greater than 1. (b) The signal-to-noise ratio associated with the optimum correlation coefficient in panel (a). (c) The optimum lead time of wind stress curl relative to WC SSIO EKE_{meso}; regions with a signal-to-noise ratio less than 1 are masked out. WC = west central; SSIO = subtropical southern Indian Ocean; EKE = eddy kinetic energy.

(Figure 12b), and only about 5–10 cm^2/s^2 is associated with cyclones (Figure 12c). The energy propagation characteristics associated with anticyclones versus cyclones also appear to be different: A tongue of elevated EKE_{meso} from anticyclones (60–80 cm^2/s^2) originates outside the box, between 90° and 100°E (Figure 12b). In contrast, a similar tongue from cyclones contains only about 30–50 cm^2/s^2 of time mean EKE_{meso} (Figure 12c). Hence, conditions appear to be more favorable for EKE_{meso} propagation into the region from anticyclones, whereas more cyclonic EKE_{meso} is generated locally in the west central SSIO.

3.3.2. Forcing Associated With Local PV Gradients

Earlier studies of the ID variability of EKE in the SSIO region (Jia, Wu, Lan, & Qiu, 2011; Zheng et al., 2018) have focused on the vertical shear of horizontal velocity ($\partial u/\partial z$ and $\partial v/\partial z$) as an indicator of favorable conditions

for baroclinic instability. Here we consider the magnitude of the lateral (horizontal) density gradient $\nabla_H \rho$, which is related to $\partial u/\partial z$ and $\partial v/\partial z$ by the thermal wind relation. We also consider the role of the potential vorticity (PV) structure in facilitating conditions for baroclinic instability, specifically the Ertel PV equal to $(f + \zeta)(-\partial \rho_\theta / \partial z)$ with potential density ρ_θ. Figure 13 illustrates an ideal setup for baroclinic instability in a Southern Hemisphere ocean setting. A steep stratification just below the mixed layer is associated with very negative PV; following isopycnal surfaces below and equatorward of this area, the along-isopycnal meridional (AIM) gradient of PV $\mathrm{d(PV)}/\mathrm{d}y > 0$ until it reaches a maximum along the isopycnal and the AIM gradient reverses sign, becoming negative. The potential exists for parcels of similar potential density and PV to be exchanged along the sloping isopycnals; hence, zero crossings in the AIM gradient of PV are a necessary (though not sufficient) condition for baroclinic instability.

In the west central SSIO, lateral density gradient magnitudes (and, by implication, local available potential energy) are maximized near 25°S at the center of the SSIO eddy band (Figures 14a and 14b). However, the difference between the gradients leading into high versus low $\mathrm{EKE_{meso}}$ periods is not sufficient to explain the variability of $\mathrm{EKE_{meso}}$ (Figure 14c). This finding differs from the results of Jia, Wu, Lan, and Qiu (2011) and Zheng et al. (2018), which may result from our focus (60°–90°E) being further west than the other studies, and/or differences in the data assimilation product used. In our analysis based on ECCO2, the most compelling mechanism to generate higher $\mathrm{EKE_{meso}}$ in the west central SSIO is a positive PV anomaly at the southern edge of the eddy band (Figure 14f), resulting in a thicker layer of (mildly) negative AIM PV gradients (Figure 14i) in which parcels can be exchanged with the positive AIM PV gradients above (Figure 14g). As PV is essentially determined by stratification in this region, a positive PV anomaly is associated with weaker stratification, that is, vertical expansion of a given layer.

The positive PV anomaly near and just south of 30°S associated with higher $\mathrm{EKE_{meso}}$ levels is located near the surface, and hence, it is likely to be forced by surface winds or heat/freshwater fluxes. An optimum correlation analysis of CCMP wind stress curl with west central SSIO $\mathrm{EKE_{meso}}$ implies that the positive PV originates from wind stress forcing (Figure 15). A band of wind stress curl just south of the eddy band is positively correlated with and leads WC SSIO $\mathrm{EKE_{meso}}$ by ~6 months (Figure 15). Two other bands of wind stress curl (within and just north of the SSIO eddy band) are negatively correlated with WC SSIO $\mathrm{EKE_{meso}}$. However, the lead times are too short (zero) or long (~1 year) to effectively explain changes in local eddy generation (Figure 15c), and PV composite anomalies in these areas are only weakly negative (Figure 14f). Hence, the positive PV forcing from wind stress curl south of 30°S appears to be the most direct pathway for atmospheric variability to increase eddy generation in the west central SSIO.

3.3.3. Possible Remote Pathway for Interior SSIO Eddy Forcing

While section 3.3.2 highlights a mechanism for local generation of mesoscale EKE variability in the west central SSIO, this does not preclude the possibility that some of the EKE variability has remote origins, and previous studies of SSIO EKE variability (Jia, Wu, Lan, & Qiu, 2011; Zheng et al., 2018) suggest that some EKE variability in the central SSIO originates further east. Moreover, a lagged correlation analysis of mesoscale EKE elsewhere in the region leading west central SSIO $\mathrm{EKE_{meso}}$ indicates an unexpectedly strong relationship between mesoscale EKE southwest of Australia and in the west central SSIO, with the variability southwest of Australia leading the west central SSIO by 2 years (Figures 16a and 16b). The correlation is weaker in the 12- to 18-month range (Figures 16c–16f) but still implies a propagation of variability northwestward toward the west central SSIO. The correlation becomes quite robust again with a 6-month lead time (Figures 16g and 16h), and maximum values of the correlation focused near the southeast corner of the box, consistent with a northwestward propagation of eddy energy, for example, by anticyclones. Moreover, a time series comparison of $\mathrm{EKE_{meso}}$ in the two regions (Figure 16j) does show peaks in $\mathrm{EKE_{meso}}$ southwest of Australia (1994–1995, 2000–2001, 2008–2009, and 2011–2012) that appear to lead peaks in activity in the west central SSIO by about 2 years.

Are individual eddies capable of conveying mesoscale EKE variations from the southwest corner of Australia to the west central SSIO? Anticyclonic eddies from southwest of Australia generally propagate in a direction toward the west central SSIO, but only a few actually reach the west central SSIO (Figure 16i), and the $\mathrm{EKE_{meso}}$ associated with these tracks (not shown) is fairly negligible. Hence, we consider the possibility that the mesoscale EKE variability in both regions is linked via the propagation of potential density and PV anomalies in the interior ocean. Elevated eddy activity in the west central SSIO is associated with a negative potential density anomaly in the lower part of the pycnocline (200- to 350-m depth), but at longer lead times is also preceded by a negative potential density anomaly near the southwest corner of Australia (Figures 17a–17c). These potential density anomalies are associated with PV and AIM PV gradient anomalies that likewise appear

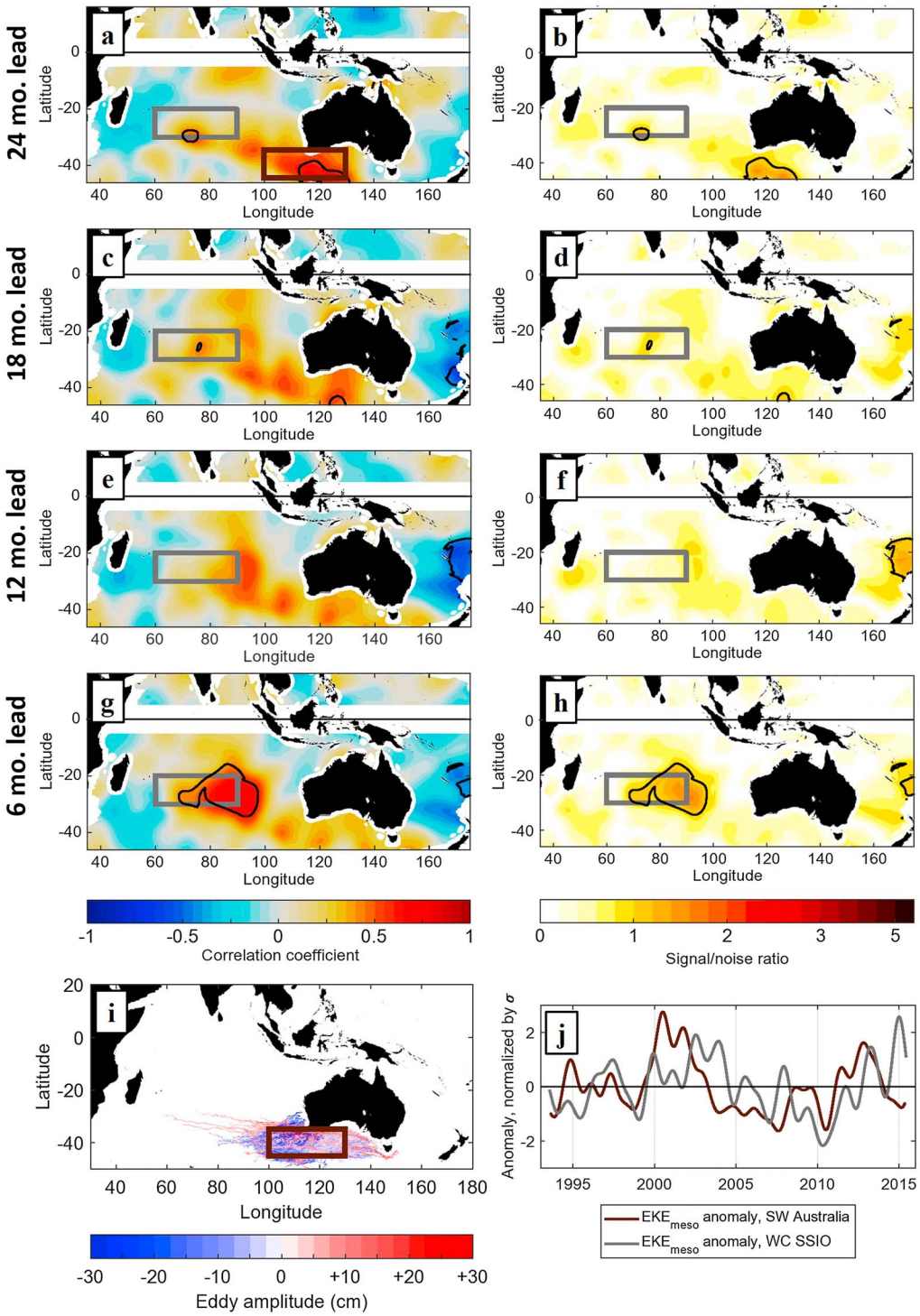

Figure 16. (a) Correlation coefficient of EKE_{meso} around the Indian Ocean region with EKE_{meso} averaged in the west central SSIO box (shaded in gray), at ID frequencies, with regional EKE_{meso} leading box-averaged west central EKE_{meso} by 24 months. The regional EKE_{meso} field was spatially smoothed with a 5° *e*-folding radius, 10° cutoff radius prior to computation of the correlations. (b) Signal-to-noise ratio of the correlation coefficient in (a), based on the distribution of correlations of normally distributed time series. (c–h) Same as (a) and (b) but for regional EKE_{meso} leading box-averaged EKE_{meso} by (c, d) 18, (e, f) 12, and (g, h) 6 months. (i) Eddy tracks of time length ≥16 weeks that pass through any part of the SW Australia region (brown box). (j) Time series comparison of EKE_{meso} in the WC SSIO and SW Australia boxes, filtered for ID frequencies and normalized by their standard deviations. ID = interannual and decadal; EKE = eddy kinetic energy; WC = west central; SSIO = subtropical southern Indian Ocean.

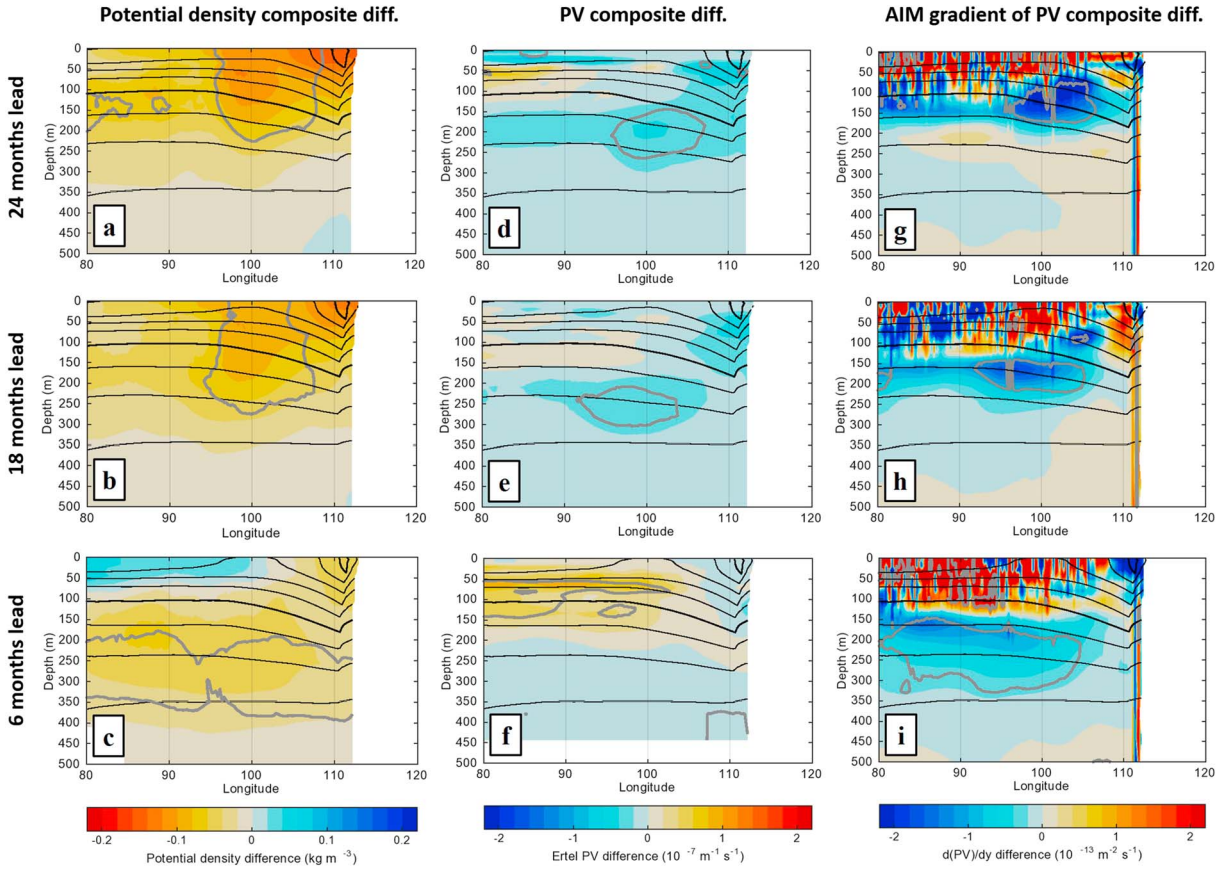

Figure 17. (a–c) Composite differences for potential density leading high WC SSIO EKE_{meso} minus low WC SSIO EKE_{meso} periods. Values are meridionally averaged 35°–25°S, overlapping with the southern part of the SSIO eddy band. Lead times for the composites are indicated on the left, and gray contours enclose differences that have a signal-to-noise ratio exceeding 1. (d–i) Same as (a)–(c), but for composite differences of (d–f) PV and (g–i) the along-isopycnal meridional PV gradient. PV = potential vorticity; WC = west central; SSIO = subtropical southern Indian Ocean; EKE = eddy kinetic energy.

to originate near southwest Australia: A near-surface negative PV anomaly off the coast of Australia moves deeper and westward at 18- to 24-month lead time, while a positive PV anomaly develops closer to the surface in the central SSIO (Figures 17d–17f). Both PV anomalies are associated with negative AIM PV gradient anomalies that propagate westward and towards increasing depths (Figures 17g–17i). Near Australia the negative AIM PV gradient anomalies also extend well south of 35°S (not shown), where they likely contribute to eddy generation southwest of Australia. The mechanism for producing negative potential density and PV anomalies off the Australian coast is less clear; wind stress curl is unlikely to be the cause, as Ekman-induced downwelling would typically result in less dense water near the surface, but also a positive PV anomaly in the Southern Hemisphere. According to similar composites of meridional velocity (not shown), Leeuwin Current variability does not have a clear link to interior mesoscale EKE, despite the effect of the current on density and stratification near the Australian coast. We did not explore whether surface heat or freshwater fluxes might force the potential density and PV anomalies in Figures 17a–17f; an anomalous heat or freshwater input into the surface ocean would produce both negative potential density and PV anomalies, and this could be a germane topic for future research.

4. Conclusions

Using satellite altimetry data for the period of 1993–2015, we identified positive correlations between mesoscale EKE and large-scale SLA in the subtropical southeast Indian Ocean from interannual to multidecadal time scales. Such covariability extends from the west coast of Australia to 80°–100°E, depending on latitude. The 24-year positive linear trends of EKE also correspond to elevated positive SLA trends across the SSIO eddy band. We did not find evidence that a preference of anticyclonic versus cyclonic eddy variability was the cause of this EKE-SLA covariability. Instead, the covariability was attributed to common remote

forcing from the tropical Pacific sector associated with ENSO and PDO that force the EKE and SLA of the southeast Indian Ocean. Wave propagation through the Indonesian Archipelago and the subsequent impacts on the SLA and eddies of the Leeuwin Current provides the conduit to transmit the effects of tropical Pacific forcing to EKE and SLA in the subtropical southeast Indian Ocean. Although EKE variability in the subtropical southeast Indian Ocean has been linked to interannual forcing from the tropical Pacific (e.g., Zheng et al., 2018), our results show that a similar remote forcing mechanism is at work on decadal time scales and for the multidecadal trend. Moreover, the EKE-SLA covariability is a new feature that has not been documented previously.

In the west central SSIO, climate mode forcing cannot explain the interannual to decadal variability of mesoscale EKE well. Positive (anticyclonic) wind stress curl forcing just south of the enhanced eddy band forces PV anomalies that affect conditions for instability in this region. Moreover, evidence is found for remote forcing of the mesoscale eddy variability in the west central SSIO via the propagation of potential density and PV gradient anomalies from the region southwest of Australia; these potential density and PV gradient anomalies also may influence eddy generation locally near Australia south of 35°S.

The covariability of the mesoscale eddy activity and large-scale sea level in the subtropical southeast Indian Ocean could influence mixed-layer heat and freshwater budgets, water-mass formation, and marine biogeochemistry. Therefore, our study motivates future research on these potential impacts. Moreover, the multidecadal trends of SLA and EKE identified in this study agree with the recent strengthening of tropical Pacific trade winds (L'Heureux et al., 2013) and associated sea level rise in the northwestern tropical Pacific (Hamlington et al., 2013; Merrifield, 2011). However, under the scenario of anthropogenic climate change, tropical Pacific trade winds are expected to weaken due to the projected slowdown of the Walker circulation (Vecchi et al., 2006). This would reduce the sea level in the western tropical Pacific, indicating that eastern SSIO SLA and EKE would also decrease unless counteracted by local forcing. Finally, our results and the related processes identified are useful for evaluating climate models, especially as global coupled model simulations begin to permit the generation of oceanic mesoscale eddies.

Acknowledgments

The research described in this paper was carried out at the Jet Propulsion Laboratory, California Institute of Technology, under contract with NASA and was supported in part by the NASA Postdoctoral Program administered by the Universities Space Research Association (USRA) under contract with NASA. Bo Qiu was supported by NASA grant NNX17AH33G. The altimeter products were produced by Collecte Localisation Satellites (CLS) with support from CNES and distributed by AVISO; presently, these data are available through the Copernicus Marine Service (http://marine.copernicus.eu). Time series of the climate indices (Niño3.4, SAM, and PDO) are available from the National Weather Service's Climate Prediction Center (http://www.cpc.ncep.noaa.gov), and the Mesoscale Eddy Trajectory Atlas product is currently available through AVISO+ (https://www.aviso.altimetry.fr). The 3-day averaged output from ECCO2 interpolated onto a 1/4° latitude/longitude grid is available from the ECCO2 website hosted by the Jet Propulsion Laboratory (http://ecco2.jpl.nasa.gov).The authors would like to thank an anonymous reviewer and Yukio Masumoto for very helpful feedback that improved this manuscript.

References

Atlas, R., Hoffman, R. N., Ardizzone, J., Leidner, S. M., Jusem, J. C., Smith, D. K., & Gombos, D. (2011). A cross–calibrated, multiplatform ocean surface wind velocity product for meteorological and oceanographic applications. *Bulletin of the American Meteorological Society*, *92*, 157–174.

Batteen, M. L., & Butler, C. L. (1998). Modeling studies of the Leeuwin Current off western and southern Australia. *Journal of Physical Oceanography*, *28*, 2199–2221.

Birol, F., & Morrow, R. (2001). Source of the baroclinic waves in the southeast Indian Ocean. *Journal of Geophysical Research*, *106*, 9145–9160.

Birol, F., & Morrow, R. (2003). Separation of quasi–semiannual Rossby waves from the eastern boundary of the Indian Ocean. *Journal of Marine Research*, *61*, 707–723.

Cai, W., Meyers, G., & Shi, G. (2005). Transmission of ENSO signal to the Indian Ocean. *Geophysical Research Letters*, *32*, L05616. https://doi.org/10.1029/2004GL021736

Chelton, D. B., Schlax, M. G., & Samelson, R. M. (2011). Global observations of nonlinear mesoscale eddies. *Progress in Oceanography*, *91*, 167–216.

Chelton, D. B., & Xie, S.-P. (2010). Coupled ocean–atmosphere interaction at oceanic mesoscales. *Oceanography*, *23*(4), 52–69.

Ducet, N., Traon, P. Y. L., & Reverdin, G. (2000). Global high–resolution mapping of ocean circulation from TOPEX/Poseidon and ERS–1 and –2. *Journal of Geophysical Research*, *105*, 19,477–19,498.

Fang, F., & Morrow, R. (2003). Evolution, movement and decay of warm–core Leeuwin Current eddies. *Deep-Sea Research Part II*, *50*, 2245–2261.

Feng, M., Meyers, G., Pearce, A., & Wijffels, S. (2003). Annual and interannual variations of the Leeuwin Current at 32°S. *Journal of Geophysical Research*, *108*(C11), 3355. https://doi.org/10.1029/2002JC001763

Feng, M., Wijffels, S., Godfrey, S., & Meyers, G. (2005). Do eddies play a role in the momentum balance of the Leeuwin Current? *Journal of Physical Oceanography*, *35*, 964–975.

Fu, L.-L. (2009). Pattern and velocity of the global ocean eddy variability. *Journal of Geophysical Research*, *114*, C11017. https://doi.org/10.1029/2009JC005349

Gaube, P., Chelton, D. B., Samelson, R. M., Schlax, M. G., & O'Neill, L. W. (2015). Satellite observations of mesoscale eddy-induced Ekman pumping. *Journal of Physical Oceanography*, *45*, 104–132.

Gaube, P., Chelton, D. B., Strutton, P. G., & Behrenfeld, M. J. (2013). Satellite observations of chlorophyll, phytoplankton biomass, and Ekman pumping in nonlinear mesoscale eddies. *Journal of Geophysical Research: Oceans*, *118*, 6349–6370. https://doi.org/10.1002/2013JC009027

Gaube, P., McGillicuddy, D. J. Jr, Chelton, D. B., Behrenfeld, M. J., & Strutton, P. G. (2014). Regional variations in the influence of mesoscale eddies on near-surface chlorophyll. *Journal of Geophysical Research: Oceans*, *119*, 8195–8220. https://doi.org/10.1002/2014JC010111

Halkides, D., & Lee, T. (2011). Mechanisms controlling seasonal mixed layer temperature and salinity in the southwestern tropical Indian Ocean. *Dynamics of Atmospheres and Oceans*, *51*, 77–93.

Hamlington, B. D., Leben, R., Strassburg, M. W., Nerem, R. S., & Kim, K.-Y. (2013). Contribution of the Pacific Decadal Oscillation to global mean sea level trends. *Geophysical Research Letters*, *40*, 5171–5175. https://doi.org/10.1002/grl.50950

Jia, F., Wu, L., Lan, J., & Qiu, B. (2011). Interannual modulation of eddy kinetic energy in the southeast Indian Ocean by Southern Annular Mode. *Journal of Geophysical Research*, *116*, C02029. https://doi.org/10.1029/2010JC006699

Jia, F., Wu, L., & Qiu, B. (2011). Seasonal modulation of eddy kinetic energy and its formation mechanism in the southeast Indian Ocean. *Journal of Physical Oceanography*, *41*, 657–665.
L'Heureux, M. L., Lee, S., & Lyon, B. (2013). Recent multidecadal strengthening of the Walker circulation across the tropical Pacific. *Nature Climate Change*, *3*, 571–576. https://doi.org/10.1038/nclimate1840
Lee, T. (2004). Decadal weakening of the shallow overturning circulation in the South Indian Ocean. *Journal of Geophysical Research*, *31*, L18305. https://doi.org/10.1029/2004GL020884
Lee, T., & Fukumori, I. (2003). Interannual-to-decadal variations of tropical-subtropical exchange in the Pacific Ocean: Boundary versus interior pycnocline transports. *Journal of Climate*, *16*, 4022–4042.
Lee, T., & Marotzke, J. (1998). Seasonal cycles of meridional overturning and heat transport of the Indian Ocean. *Journal of Physical Oceanography*, *28*, 923–943.
Lee, T., & McPhaden, M. J. (2008). Decadal phase changes in large–scale sea level and winds in the Indo–Pacific region at the end of the 20th century. *Geophysical Research Letters*, *35*, L01605. https://doi.org/10.1029/2007GL032419
Mantua, N. J., Hare, S. R., Zhang, Y., Wallace, J. M., & Francis, R. C. (1997). A Pacific interdecadal climate oscillation with impacts on salmon production. *Bulletin of the American Meteorological Society*, *78*(6), 1069–1079.
Marshall, J., Adcroft, A., Hill, C., Perelman, L., & Heisey, C. (1997). A finite-volume, incompressible Navier Stokes model for studies of the ocean on parallel computers. *Journal of Geophysical Research*, *102*(C3), 5753–5766.
Melnichenko, O., Amores, A., Maximenko, N., Hacker, P., & Potemra, J. (2017). Signature of mesoscale eddies in satellite sea surface salinity data. *Journal of Geophysical Research: Oceans*, *122*, 1416–1424. https://doi.org/10.1002/2016JC012420
Menemenlis, D., Campin, J., Heimbach, P., Hill, C., Lee, T., Nguyen, A., et al. (2008). ECCO2: High resolution global ocean and sea ice data synthesis. *Mercator Ocean Quarterly Newsletter*, *31*, 13–21.
Menemenlis, D., Fukumori, I., & Lee, T. (2005). Using Green's functions to calibrate an ocean general circulation model. *Monthly Weather Review*, *133*(5), 1224–1240.
Menemenlis, D., Hill, C., Adcroft, A., Campin, J.-M., Cheng, B., Ciotti, B., et al. (2005). NASA supercomputer improves prospects for ocean climate research. *Eos Transactions American Geophysical Union*, *86*(9), 89–96.
Menezes, V. V., Phillips, H. E., Schiller, A., Bindoff, N. L., Domingues, C. M., & Vianna, M. L. (2014). South Indian Countercurrent and associated fronts. *Journal of Geophysical Research: Oceans*, *119*, 6763–6791. https://doi.org/10.1002/2014JC010076
Menezes, V. V., Phillips, H. E., Vianna, M. L., & Bindoff, N. L. (2016). Interannual variability of the South Indian Countercurrent. *Journal of Geophysical Research: Oceans*, *121*, 3465–3487. https://doi.org/10.1002/2015JC011417
Merrifield, M. A. (2011). A shift in western tropical Pacific sea level trends during the 1990s. *Journal of Climate*, *24*, 4126–4138.
Morrow, R., & Birol, F. (1998). Variability in the southeast Indian Ocean from altimetry: Forcing mechanisms for the Leeuwin Current. *Journal of Geophysical Research*, *103*, 18,529–18,544.
Morrow, R., Birol, F., Griffin, D., & Sudre, J. (2004). Divergent pathways of cyclonic and anti-cyclonic eddies. *Geophysical Research Letters*, *31*, L24311. https://doi.org/10.1029/2004GL020974
Morrow, R., Fang, F., Fieux, M., & Molcard, R. (2003). Anatomy of three warm-core Leeuwin Current eddies. *Deep-Sea Research Part II*, *50*, 2229–2243.
Palastanga, V., van Leeuwen, P. J., & de Ruijter, W. P. M. (2006). A link between low-frequency mesoscale eddy variability around Madagascar and the large-scale Indian Ocean variability. *Journal of Geophysical Research*, *111*, C09029. https://doi.org/10.1029/2005JC003081
Palastanga, V., van Leeuwen, P. J., Schouten, M. W., & de Ruijter, W. P. M. (2007). Flow structure and variability in the sub-tropical Indian Ocean: Instability of the South Indian Ocean Countercurrent. *Journal of Geophysical Research*, *112*, C01001. https://doi.org/10.1029/2005JC003395
Potemra, J. T. (2001). Contribution of equatorial Pacific winds to southern tropical Indian Ocean Rossby waves. *Journal of Geophysical Research*, *106*, 2407–2422.
Qiu, B., Chen, S., Wu, L., & Kida, S. (2015). Wind- versus eddy-forced regional sea level trends and variability in the North Pacific Ocean. *Journal of Climate*, *28*, 1561–1577.
Saji, N. H., Goswami, B. N., Vinayachandran, P. N., & Yamagata, T. (1999). A dipole mode in the tropical Indian Ocean. *Nature*, *401*, 360–363.
Schott, F. A., Dengler, M., & Schoenefeldt, R. (2002). The shallow overturning circulation of the Indian Ocean. *Progress in Oceanography*, *53*, 57–103.
Smith, R. L., Huyer, A., Godfrey, J. S., & Church, J. A. (1991). The Leeuwin Current off western Australia, 1986–1987. *Journal of Physical Oceanography*, *21*, 323–345.
Thompson, R. O. R. Y. (1987). Continental-shelf-scale model of the Leeuwin Current. *Journal of Marine Research*, *45*, 813–827.
Thompson, K. R., & Demirov, E. (2006). Skewness of sea level variability of the world's oceans. *Journal of Geophysical Research*, *111*, C05005. https://doi.org/10.1029/2004JC002839
Trenary, L. L., & Han, W. (2012). Intraseasonal-to-interannual variability of south Indian Ocean sea level and thermocline: Remote versus local forcing. *Journal of Physical Oceanography*, *42*, 602–627.
Trenary, L. L., & Han, W. (2013). Local and remote forcing of decadal sea level and thermocline depth variability in the South Indian Ocean. *Journal of Geophysical Research: Oceans*, *118*, 381–398.
Vecchi, G. A., Soden, B. J., Wittenberg, A. T., Held, I. M., Leetmaa, A., & Harrison, M. J. (2006). Weakening of tropical Pacific atmospheric circulation due to anthropogenic forcing. *Nature*, *441*, 73–76.
Wijffels, S., & Meyers, G. (2004). An intersection of oceanic waveguides: Variability in the Indonesian Throughflow region. *Journal of Physical Oceanography*, *34*, 1232–1253.
Xie, S.-P., Annamalai, H., Schott, F. A., & McCreary, J. P. Jr (2002). Structure and mechanism of south Indian Ocean climate variability. *Journal of Climate*, *15*, 864–878.
Zheng, S., Du, Y., Li, J., & Cheng, X. (2015). Eddy characteristics in the South Indian Ocean as inferred from surface drifters. *Ocean Science*, *11*, 361–371.
Zheng, S., Feng, M., Du, Y., Meng, X., & Yu, W. (2018). Interannual variability of eddy kinetic energy in the subtropical southeast Indian Ocean associated with the El Niño–Southern Oscillation. *Journal of Geophysical Research: Oceans*, *123*, 1048–1061. https://doi.org/10.1002/2017JC013562